

Influence of Outcrop Scale Fractures on the Effective Stiffness of Fault Damage Zone Rocks

W. ASHLEY GRIFFITH,^{1,3} PABLO F. SANZ,^{2,4} and DAVID D. POLLARD¹

Abstract—We combine detailed mapping and microstructural analyses of small fault zones in granodiorite with numerical mechanical models to estimate the effect of mesoscopic (outcrop-scale) damage zone fractures on the effective stiffness of the fault zone rocks. The Bear Creek fault zones were active at depths between 4 and 15 km and localize mesoscopic off-fault damage into tabular zones between two subparallel boundary faults, producing a fracture-induced material contrast across the boundary faults with softer rocks between the boundary faults and intact granodiorite outside the boundary faults. Using digitized fault zone fracture maps as the modeled fault geometries, we conduct nonlinear uniaxial compression tests using a novel finite-element method code as the experimental “laboratory” apparatus. Map measurements show that the fault zones have high nondimensional fracture densities (>1), and damage zone fractures anastomose and intersect, making existing analytical effective medium models inadequate for estimation of the effective elastic properties. Numerical experiments show that the damage zone is strongly anisotropic and the bulk response of the fault zone is strain-weakening. Normal strains as small as 2% can induce a reduction of the overall stiffness of up to 75%. Fracture-induced effective stiffness changes are large enough to locally be greater than intact modulus changes across the fault due to juxtaposition of rocks of different lithologies; therefore mesoscopic fracturing is as important as rock type when considering material or bimaterial effects on earthquake mechanics. These results have important implications for earthquake rupture mechanics models, because mesoscopic damage zone fractures can cause a material contrast across the faults as large as any lithology-based material contrast at seismogenic depths, and the effective moduli can be highly variable during a single rupture event.

Key words: Damage zone, effective medium, Young’s modulus, finite-element method, bimaterial.

1. Introduction

Fault zones are heterogeneous structures. In some cases, this heterogeneity can be inherited and may be related either to rock lithology or preexisting structural elements (e.g., BERGBAUER and MARTEL, 1999; DAVATZES and AYDIN, 2003; MYERS and AYDIN, 2004;

¹ Department of Geological and Environmental Sciences, Stanford University, Stanford, CA, 94305 U.S.A.
E-mail: dpollard@stanford.edu

² Civil and Environmental Engineering, Stanford University, Stanford, CA, 94305 U.S.A.
E-mail: pablo.f.sanz@exxonmobil.com

³ Istituto Nazionale di Geofisica e Vulcanologia, Via di Vigna Murata, 605, 00143-Roma, Italia.
E-mail: griffith@ingv.it

⁴ ExxonMobil Upstream Research Company.

SEGALL and POLLARD, 1983a, 1983b). Also, heterogeneity is commonly related to the processes responsible for fault growth, slip, and evolution: Rocks adjacent to faults are typically fractured due to brittle deformation associated with repeated slip events on the main fault surface(s).

Together, the primary fault surface and the adjacent, fractured rocks comprise two structural domains of the most commonly acknowledged idealization of a fault zone (e.g., CHESTER *et al.*, 1993): (1) *the fault core* and (2) *the damage zone*. The fault core typically consists of highly comminuted and altered rock and hosts most of the shear deformation along one or more principal slip zones (e.g., CHESTER and CHESTER, 1998). The damage zone can be symmetric or asymmetric about the fault core, and typically consists of variably fractured rock where microscopic and macroscopic fracture density increases with proximity to the fault core (e.g., CHESTER *et al.*, 2004; SCHULTZ and EVANS, 2000).

The structure of fault zones in the Mt. Abbot quadrangle (Fig. 1) of the central Sierra Nevada (e.g., MARTEL, 1990; MARTEL and BOGER, 1998; MARTEL and POLLARD, 1989; MARTEL *et al.*, 1988; PACHELL and EVANS, 2002) deviate from this idealized fault zone model. Individual small faults typically consist of a thin fault core, <1–2 cm in thickness, surrounded by granodiorites largely undamaged except for wing cracks concentrated around the fault tips (SEGALL and POLLARD, 1983a). In more mature fault zones, the subject of this study, total offset is typically on the order of several meters to >100 meters, and damage in the form of outcrop-scale fractures is concentrated between paired faults, and rocks immediately outside of the paired faults are largely undamaged (Fig. 1).

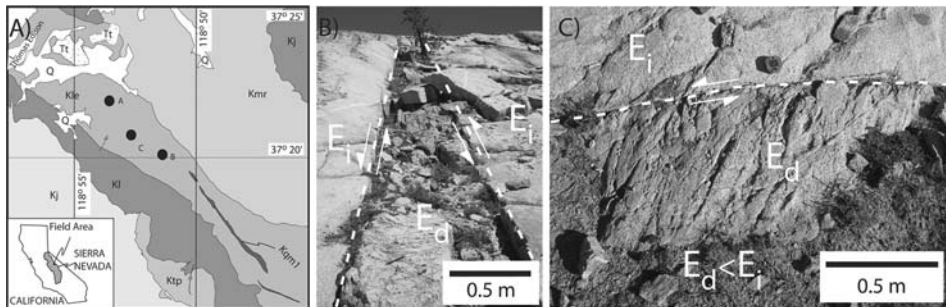


Figure 1

(A) Simplified geological map of a portion of the Bear Creek drainage (modified from BERGBAUER and MARTEL, 1999; GRIFFITH *et al.*, 2008; and LOCKWOOD and LYDON, 1975). The main geologic units shown are, from oldest to youngest, unspecified Cretaceous and Jurassic plutons (Kj), the Lamarck Granodiorite (Kl), the Mount Givens Granodiorite (Kmo), the Lake Edison Granodiorite (Kle), Quartz monzonite of Mono Recesses (Kmr), Cretaceous quartz monzonite and granite (Kqm1), Granitic rock of uncertain affinity (Ktp), Tertiary olivine trachybasalt (Tt), and Quaternary deposits (Q). Black circles and letter designations A–C refer to the locations of top, middle, and bottom fault zone maps illustrated in Figure 3. (B) and (C) Fault zones consist of discrete subvertical left-lateral boundary faults (E_i) with damage in the form of outcrop-scale cross fractures localized between. Extensive damage is confined to the region between the boundary faults, and rocks outside of the boundary faults are typically intact. The fault zone in (A) is approximately 1 meter wide. Only one boundary fault is exposed in the fault zone pictured in (B). The stiffness E_d of the damaged granodiorite is expected to be less than the stiffness E_i of the intact granodiorite.

Increased fracture density leads to a decrease in the effective uniaxial stiffness (FAULKNER *et al.*, 2006; WALSH, 1965) and strength (LOCKNER *et al.*, 2000) of the damage zone rocks. The effective stiffnesses, or moduli, describe the stress-strain responses of fault zone materials. Changes in the effective moduli during fault zone evolution have important implications for the mechanics of slip events that occur on them. The effective elastic moduli of rocks have been shown theoretically and experimentally to influence a number of earthquake phenomena including, but not limited to:

- (i) Velocity of shear ruptures. The shear modulus of fault rocks limits the rupture velocity of earthquakes: Off-fault damage has been shown to slow earthquake rupture significantly in laboratory experiments (e.g., BIEGEL *et al.*, 2008). In undamaged materials the limiting velocity for ‘subshear’ ruptures is $\sim 92\%$ of the shear-wave velocity (v_s) where $v_s = \sqrt{G/\rho}$ and G is the shear modulus and ρ is the mass density.
- (ii) Directivity of earthquake ruptures on faults that juxtapose dissimilar materials. Juxtaposition of rocks with different elastic moduli across a fault interface may influence the directivity of pulse-like ruptures if the contrast is great enough: ANDREWS and BEN-ZION (1997) showed that for a two-dimensional plain strain mode II rupture on a bimaterial interface with a constant coefficient of friction, slip pulses propagate in the direction of slip in the more compliant medium when the wave-speed contrast between the media is 20% or greater. While some doubt has been cast on the importance of this mechanism for rupture directivity in nature, due to effects related to time-weakening friction and three-dimensional rupture (ANDREWS and HARRIS, 2005; HARRIS and DAY, 2005; XIA *et al.*, 2005), the bimaterial mechanism might be relevant for primarily mode II ruptures (AMPUERO and BEN-ZION, 2008; BEN-ZION, 2006a, 2006b). DOR *et al.* (2006) examined damage distributions around several large faults and concluded that asymmetrically distributed damage, where more damage occurs on the stiffer side of the fault, was consistent with repeated unilateral ruptures over time with the same directivity. However, damage created by repeated unilateral ruptures may alter the effective modulus of the originally stiffer rocks.
- (iii) Balance between heat production and thermal pressurization of pore fluids during faulting. Damage zone fracturing can work against thermal pressurization during earthquake ruptures by increasing the effective compressibility of the fault zone rocks (e.g., LACHENBRUCH, 1980; MASE and SMITH, 1987; NODA and SHIMAMOTO, 2005; RICE, 2006; SIBSON, 1973). Recent studies have used laboratory measurements of cylindrical samples taken from fault zones to constrain model values of compressibility (e.g., RICE, 2006; WIBBERLEY, 2002). If fault wall rocks are heavily fractured, however, their bulk compressibility is expected to differ relative to that of undamaged rocks (e.g., WALSH, 1965).

In mechanical studies, fault zones are commonly idealized as a discrete discontinuity or a thin shearing layer between identical or dissimilar isotropic, homogeneous materials,

where the material, properties are assigned values believed to be representative of the entire continuum (e.g., ANDREWS and BEN-ZION, 1997; BEN-ZION and SAMMIS, 2003; POLLARD and SEGALL, 1987). Considerable attention has been given to measuring representative material parameters, including effective elastic moduli, of fault core and damage zone materials in natural fault zones (e.g., FAULKNER *et al.*, 2006; LOCKNER *et al.*, 2000; WIBBERLEY, 2002; WIBBERLEY and SHIMAMOTO, 2003) in an attempt to constrain the appropriate model material properties. These studies have confirmed the correlation between microscopic damage and alteration in fault zones and material properties such as strength and compressibility.

In addition, extensive literature has been developed regarding the analytical estimation of the properties of damaged rocks (e.g., BUDIANSKY and O'CONNELL, 1976; HUDSON, 1980; HUDSON *et al.*, 1992; KACHANOV, 1987, 1992; LYAKHOVSKY *et al.*, 1997; WALSH, 1965). However, most of these studies focus on (1) small deformations, and (2) sparse populations of small, microscopic cracks. On the other hand, slight attention has been given to the role of mesoscopic, intersecting fractures on the effective moduli of rocks in fault zones.

The three-dimensional extent of damage zones around large, crustal scale faults has been elucidated by seismological analysis of trapped waves (BEN-ZION *et al.*, 2003; LI *et al.*, 1994) and by geodesy (FIALKO, 2004). BEN-ZION *et al.* (2003) and FIALKO (2004) inferred structures that reduced the shear-wave velocity by a factor of two in damage zones on the order of 100 m and 2 km thick, respectively. In both cases the inferred damage zone exists primarily over the top few km, suggesting that extensive damage zone development is confined to the uppermost part of the crust, above the seismogenic zone (5–15 km). BEN-ZION and SHI (2005) used two-dimensional simulations of dynamic rupture on a material interface separating dissimilar materials to illustrate that increasing confining pressure tends to decrease off-fault plastic strain associated with dynamic rupture significantly at depths below about 3 km. Extensive damage zone development may be limited further at seismogenic depths by increased healing rates along faults and fractures relative to shallower depths (e.g., FINZI *et al.*, 2009, and references therein).

The goal of this study is to quantify the effect of mesoscopic fractures in small (~0.5–3 m thick) damage zones along faults exhumed from seismogenic depths (4–15 km) on the effective stiffness of the damage zone rocks. We mapped and sampled faults and damage zone fractures in granodiorites in the Bear Creek drainage of the Sierra Nevada (e.g., MARTEL *et al.*, 1988; SEGALL and POLLARD, 1983). These faults and fractures contain both hydrothermal mineral deposits and pseudotachylytes (e.g., GRIFFITH *et al.*, 2008), suggesting that they slipped under variably saturated conditions and underwent seismic deformation. We calculate the contribution of the damage zone fractures to the bulk elastic properties of the fault zones using numerical mechanical models. The models accurately represent the mapped geometry of the damage zone fractures and treat the fractures as frictional interfaces, and boundary conditions are chosen to represent expected conditions at seismogenic depths at which the faults were active.

2. Study Area

Fracturing in the Sierra Nevada batholith has been documented in the Bear Creek drainage, in the southern half of the Mount Abbot quadrangle (LOCKWOOD and LYDON, 1975; MARTEL *et al.*, 1988; SEGALL and POLLARD, 1983a.). These studies have concentrated on the Lake Edison Granodiorite (~ 88 Ma). The ages are based on K-Ar analyses of hornblende (BERGBAUER and MARTEL, 1999). The depth of emplacement of the plutons is estimated at 4–15 km based on amphibole geobarometry pressure estimates of 100–400 MPa (AGUE and BRIMHALL, 1988). Syn-to-post-magmatic structures in Bear Creek occur in the form of nearly vertical dikes, shear zones, joints, and faults. Radiometric age constraints tie the fracturing to the period immediately after plutonic intrusion during cooling and, perhaps, emplacement of adjacent plutons (BERGBAUER and MARTEL, 1999; SEGALL *et al.*, 1990; STERN *et al.*, 1981).

The faults of Bear Creek strike parallel to the joints and slipped left-laterally. Three macroscopic stages of fracturing/faulting are recognized. The first stage (Fig. 2I) is characterized by a single set of pre-faulting joints that strike predominantly ENE and are mineralized principally by quartz, epidote, and chlorite (MARTEL *et al.*, 1988; SEGALL and POLLARD, 1983a). The traces of the ENE-striking joints are as long as several tens of meters, they have opened as much as a few centimeters, and they are spaced centimeters to several meters apart. The second stage (Fig. 2II) is characterized by “small faults” (MARTEL *et al.*, 1988; SEGALL and POLLARD, 1983b), with dimensions similar to those of the joints and as much as 2 m of slip. The small faults also commonly display oblique opening mode fractures (wing cracks) near their ends (SEGALL and POLLARD, 1983a). Microstructurally, small faults record a diverse history of deformation mechanisms ranging from crystal plastic shear to brittle fracture and comminution, and frictional melting (Fig. 2A–C; GRIFFITH *et al.*, 2008). The third stage (Fig. 2III) is characterized by “simple fault zones” (MARTEL *et al.*, 1988), tabular volumes of variably fractured rock typically 0.5–3 m thick which are the subject of this study. These zones are bounded by faults ≤ 1 –2 centimeters thick that, in turn, are linked by obliquely striking fractures. The simple fault zones are as long as one kilometer, but have segments tens of meters long, similar to the lengths of the longest joints. The simple fault zones accommodate as much as 20 meters of slip, with the slip being concentrated on the boundary faults. Simple fault zones rarely coalesce into “compound fault zones” (MARTEL, 1990). These have lengths as great as several kilometers, widths as great as several meters, and accommodate up to 140 meters of slip (PACHELL and EVANS, 2002). This commonly observed hierarchy implies that the width of damage zone development along the Bear Creek faults is limited by pre-existing anisotropy, as the faults grew from subparallel cooling joints, and the damage zones are confined to tabular zones between the subparallel faults.

The damaged rock within the fault zones is variably fractured, ranging from a few discrete cross-fractures to pulverized epidote and chlorite-rich gouge (Fig. 1B, C). In the more densely fractured cases the fault zones can be identified geomorphically in the field by the presence of narrow troughs, the walls of which approximate the boundary fault

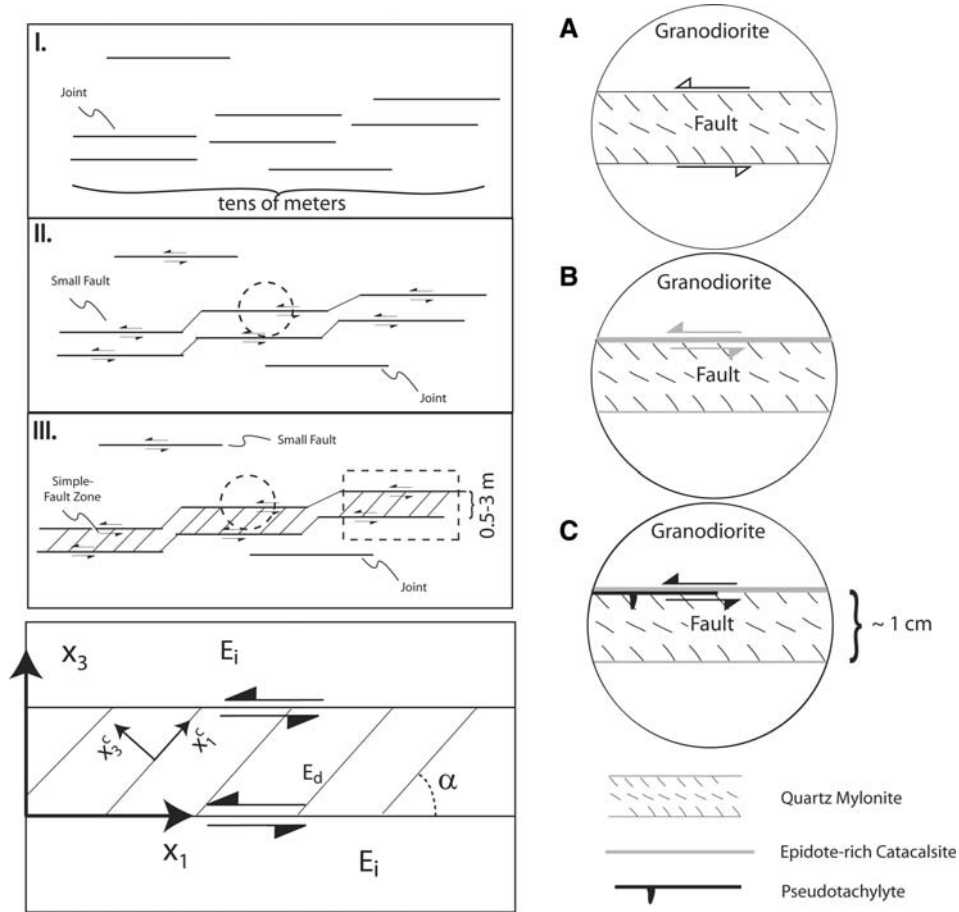


Figure 2

Conceptual model of macroscopic and microscopic evolution of faults in Bear Creek. I-III correspond to the macroscopic evolution of faults suggested by MARTEL *et al.* (1988), where in stage I joints form in response to thermal stresses; stage II is marked by slip nucleation along joints and subsequent linkage to form small faults; and in stage III simple fault zones composed of paired small faults linked by secondary fractures form due to the interaction of neighbouring faults. Dashed circles in II and III indicate the location of A, B, and C. A-C represent the microstructural evolution of faults from crystal plastic shear on quartz mylonites to cataclastic overprint and pseudotachylyte generation. Bottom left illustrates the fault zone configuration with fracture-induced effective modulus contrast between the interior damage zone rocks (E_d) and intact granodiorites (E_i) outside of the boundary faults and defines the global and crack-local reference frames.

surfaces (Fig. 1B). In rare cases, fault zones are exposed in outcrop along limited distances parallel to the strike of the boundary faults (<10 m). MARTEL *et al.* (1988) mapped and described some of these exposures. For this study we mapped and sampled two additional fault zones in the Bear Creek area, and we include a simplified version of Martel's fault zone map from the "Waterfall Site" (Fig. 3). The fault zones always

consist of two paired boundary faults, each with a left-lateral sense of shear. In less mature fault zones, the trend of cross-fractures typically makes small ($30\text{--}50^\circ$) angles with the boundary faults; however in more mature faults additional cross fractures at higher angles tend to infill the fault zones (Fig. 3A). The boundary faults are typically less than 1–2 cm in thickness (Fig. 4A), and the cross fractures are typically much less than 1 cm in thickness (Fig. 4B, C). Measured offset on cross fractures is always less

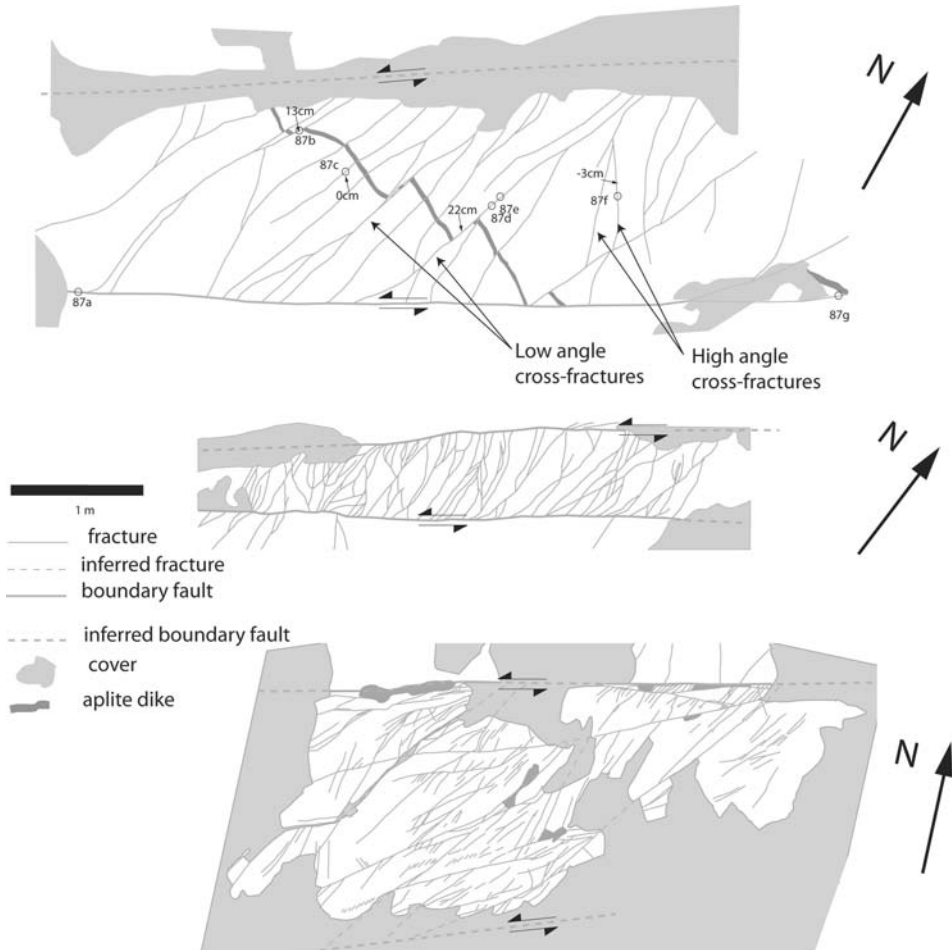


Figure 3

Three Bear Creek fault zones mapped and sampled for this study. In all cases the fault zones consist of a tabular zone with cross fractures bounded by left-lateral boundary faults. Fault zones typically accommodate up to 20 m of total offset. Top fault zone is the Big Juniper Fault Zone (BJFZ). Note offset aplite dike cutting through the entire fault zone. Middle fault zone is from the Trail Junction Meadows site of SEGAL and POLLARD (1983). Bottom fault zone is modified from the map of MARTEL *et al.* (1988) from the Waterfall site. Scale bar applies for all three mapped fault zones.

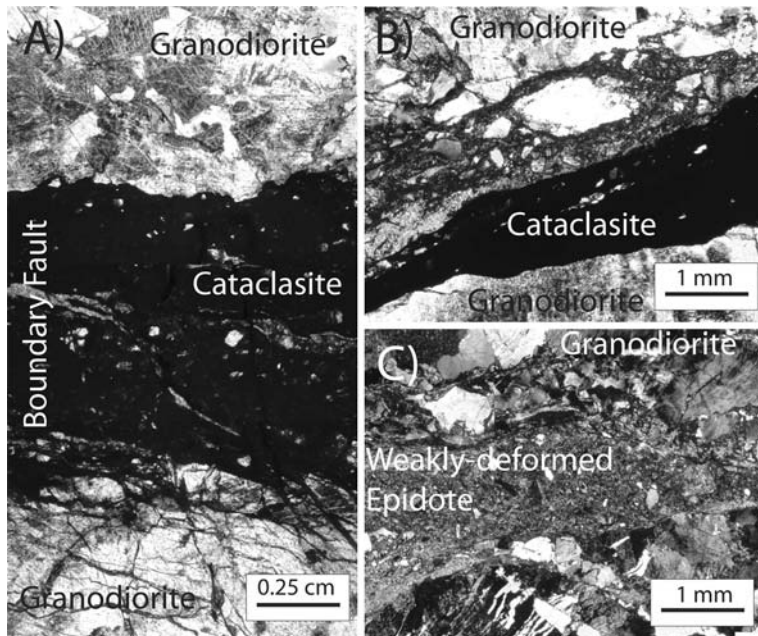


Figure 4

Microstructures of boundary faults and cross fractures. (A) Boundary fault from the BJFZ under plane polarized light. Fault consists of highly comminuted fine-grained cataclasite. This fault accommodated several meters of slip. (B) Cross fracture with 22 cm slip. Lighter colored coarse cataclasite is cut by finer grained cataclasite. (C) Cross fracture with less than 3 cm slip. Entire cataclasite zone is dominated by coarse grained, euhedral epidote and chlorite.

than that on boundary faults and can vary from zero to several tens of centimeters. Offset, if any, along low angle cross fractures is left-lateral, however fractures oriented at high angles relative to the boundary faults can show small (\leq a few centimeters) right-lateral offset.

In thin section, boundary faults contain variably comminuted grains consisting of quartz and feldspar clasts from the host rock, precursory quartz mylonites, epidote, chlorite, and minor sphene. While quartz and feldspar clasts are sourced from the host rock and precursory mylonites, epidote and chlorite were formed by fluid-rock interaction after the onset of brittle faulting (Griffith *et al.*, 2008). In fractures with little or no apparent offset ($<$ a few centimeters), epidote grains are typically prismatic in shape and show very little comminution (Fig. 4C). Qualitative analysis of thin sections suggests that slip along these faults is typically accompanied by grain size reduction and rounding of clasts (e.g., Fig. 4). In boundary faults, the core material typically consists of very fine grained cataclasite and ultracataclasite. Boundary faults and cross fractures with large measured (tens of centimeters to meters) offsets commonly show evidence of multiple principal slip zones. In the case of the cross-fracture shown in Figure 4B, an early

cataclastic fabric has been overprinted by a fine-grained ultracataclasite which is dark to opaque in plane polarized light.

Conceptual models proposed for the formation of these paired fault zones attribute the formation and localization of damage to slip on the boundary faults. MARTEL and POLLARD (1989) hypothesized that the cross fractures formed as opening mode wing cracks formed at the tips of small slip patches on the boundary faults. MARTEL and BOGER (1998) attributed the cross fractures to three-dimensional interaction between the boundary faults at overlaps near the fault's upper and lower (mode III) tips. Because of limited exposure, it is difficult to assess the along-strike continuity of fault zones, and whether damage exists between boundary faults along their entire lengths, or just near extensional step-overs along boundary faults. Regardless of the formation mechanism, a few observations are clear based on field mapping and microstructural analysis:

- (i) Damage in the form of mesoscopic fractures is consistently concentrated between thin (<1–2 cm) boundary faults, and the host granodiorite shows little mesoscopic fracturing outside of the boundary faults; and
- (ii) The cross fractures form as opening mode fractures filled variably by secondary epidote, chlorite, and clasts of the host rock. The cross fractures slipped in association with slip events on the boundary faults, resulting in comminution of fracture mineral fillings. Continued slip events along boundary faults were apparently accompanied by reactivation of existing cross fractures and by increased damage by formation of new fractures.

Continued slip on boundary faults after localization of damage on the interior of the paired fault zones results in an increasingly strong material contrast across each of the paired boundary faults, where damage within the fault zone induces an effectively softer material on the inside of the fault zone relative to the unfractured granodiorite outside of the fault zone.

3. Fault Zone Idealization

We calculate effective values for fault zone stiffness in a global reference frame where x_1 is parallel to the boundary faults and the outcrop face is parallel to the x_1 - x_3 plane (Fig. 5). For analytical calculations (Appendix A), an additional fracture-local coordinate system is centered on each fracture, with the x_3 axis orthogonal to the cross-fractures, at an angle α to the positive x_1 axis in the global reference frame (Fig. 5).

We confine the numerical investigation to the Big Juniper Fault Zone (BJFZ) shown in Figure 3A. This fault zone was chosen because abundant offset markers (including an aplite dike that transects the entire fault zone, and an offset xenolith on the antithetic fracture at sample location 87f, Fig. 3A) provide constraints on slip on several cross fractures and boundary faults. This allows us to confirm that the model reproduces the

observed slip distributions under approximate loading conditions operating when the faults were active. This confirmation is discussed in more detail in the section *Model Geometry Confirmation*. The fractured damage zone is tabular in shape and bounded by two subparallel faults. To standardize application of external boundary conditions we created a fault mesh that is rectangular in shape and represents the average width of the fault damage zone (Fig. 5). This simplification required extension of some of the cross fractures partially covered by sediment to the model boundary. A comparison of the mapped fault geometry and the model mesh is shown in Figure 6.

Here we are interested in estimating the effective elastic stiffness of fractured damage zone rocks in the reference frame defined above. The numerical simulations focus on calculating the effective apparent Young's modulus of the fault zone as a representation of the overall stiffness. In the isotropic elastic compliance tensor Young's modulus ($E = 1/s_{11} = 1/s_{22} = 1/s_{33}$) defines the relationship between an applied normal stress and the parallel normal strain under *uniaxial* stress conditions:

$$\sigma_{33} = E\varepsilon_{33}, \quad \sigma_{11} = \sigma_{22} = \sigma_{12} = \sigma_{13} = \sigma_{23} = 0. \quad (1)$$

In this case Young's modulus is defined with uniaxial loading in the x_3 direction. However, because the fault zones presented in this study are extensively fractured by cross fractures that anastomose, but are approximately subparallel, the fault zone should behave as an anisotropic body as a whole. In the case that fractures within a damaged rock consist of a single set of parallel fractures, the rock body is expected to be *transversely anisotropic*. In the crack-local reference frame (Fig. 2) where the normals to the fractures are parallel to the x_3^c axis, the compliance tensor is completely defined by five independent constants:

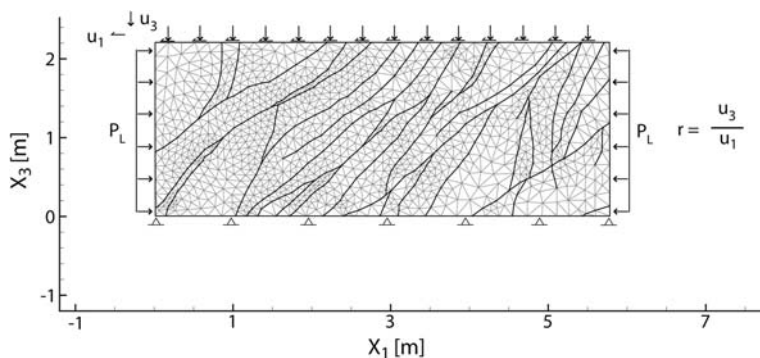


Figure 5

Discretized fault zone (BJFZ from Fig. 3) with external boundary conditions defined for the model geometry validation.

$$s_{IJ} = \begin{bmatrix} s_{11} & s_{12} & s_{13} & 0 & 0 & 0 \\ s_{12} & s_{11} & s_{13} & 0 & 0 & 0 \\ s_{13} & s_{13} & s_{33} & 0 & 0 & 0 \\ 0 & 0 & 0 & s_{44} & 0 & 0 \\ 0 & 0 & 0 & 0 & s_{44} & 0 \\ 0 & 0 & 0 & 0 & 0 & s_{66} \end{bmatrix}, \quad s_{66} = \frac{s_{11} - s_{22}}{2}. \quad (2)$$

As the compliance matrix is written above, x_3^c is the axis of symmetry. Here, the Young's modulus in the x_3^c direction is equivalent to $1/s_{33}$. If the compliance matrix is transformed by a rotation about α to the global reference frame, compliances s_{45} , s_{54} , s_{16} , s_{61} , s_{26} , and s_{62} become nonzero. In the transformed compliance tensor, S_{ij}' , $1/s_{33}'$ then represents the *apparent* Young's modulus in the x_3 direction, as principal stresses are not necessarily parallel to principal strains in this case.

4. Numerical Model

We use a finite-element method code based on continuum and contact mechanics (SANZ, 2008; SANZ *et al.*, 2007, 2008) to simulate deformation on the mapped fault geometry of the Big Juniper Fault Zone (BJFZ, Fig. 3A). The mechanical models are

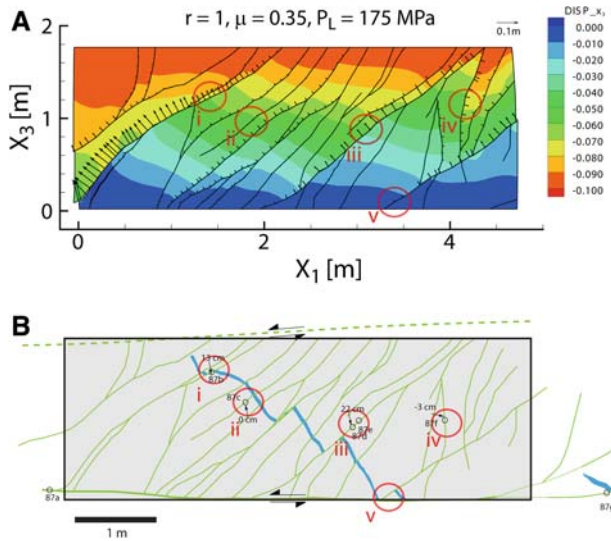


Figure 6

Comparison of numerically computed slip distributions with geological observations. (A) Slip distributions (arrows) and x_3 -parallel displacements (contours) for experiment with $r = \Delta V/\Delta H = 1$ and $\mu = 0.35$. Arrows normal to faults indicate left-lateral slip if pointing to the upper left and right-lateral slip if pointing to the lower right. Length of arrows corresponds to computed slip magnitude. (B) Mapped fault geometry with offsets along cross fractures measured in the field.

two-dimensional with plane strain assumed, and the fault zone fractures are represented as an array of material interfaces with the mapped geometry, separating isotropic, homogeneous material with constitutive properties representative of undamaged granodiorite: $E = 60 \text{ GPa}$ (BIRCH, 1966) and $\nu = 0.25$ (GERCEK, 2007). Constants and boundary conditions used in models discussed in the text are summarized in Table 1. Contact mechanics (Appendix B) enables us to model slip and/or opening on the fractures. Such relative displacements of the fracture surfaces requires frictional contact constraints along these interfaces.

A regularized Coulomb friction law simulates the mechanical response of the interfaces (Appendix B; LAURSEN and SIMO, 1993; WRIGGERS, 2002). Each contact surface has three mechanical parameters: A normal elastic stiffness k_N , a tangential elastic stiffness k_T , and a sliding friction coefficient μ . Frictional slip is path-dependent in nature and its evolution requires the integration of the constitutive law in finite steps. The integration is performed by a return-mapping algorithm similar to a non-associative plasticity model (WRIGGERS, 2002). We discretize the interfaces with node-to-segment contact elements (LAURSEN and SIMO, 1993; WRIGGERS, 2002). A more detailed discussion of the mechanical framework and of the numerical implementation can be found in Appendix B and in SANZ (2008) and SANZ *et al.* (2007).

4.1. Model Geometry Confirmation

In order to confirm that the overall model response is representative of the natural fracture system, we use geologic observations to assign boundary conditions that approximate conditions in which the faults were active and compare the resulting slip distribution to the distribution mapped in Figure 3. Because none of the internal fault zone fractures cut or offset the boundary faults in the field, we prescribe displacement

Table 1
Constants and boundary conditions imposed on numerical simulations discussed in text

Test Purpose	E , Intact (MPa)	ν , Intact	Total u_I (m)	Total u_3 (m)	σ_I (MPa)	σ_3 (MPa)	μ	k_T (GPa/m)	k_N (GPa/m)
Geometry Confirmation $r = 1$	60	0.25	0.25*	0.25	$P_L = 175$	-	0.35	10,000	10,000
$E_1 (\mu = 0.3)$	60	0.25	0.1	-	-	$P_L = 175$	0.3	10,000	10,000
$E_1 (\mu = 0.5)$	60	0.25	0.1	-	-	$P_L = 175$	0.5	10,000	10,000
$E_1 (\mu = 0.7)$	60	0.25	0.1	-	-	$P_L = 175$	0.7	10,000	10,000
$E_3 (\mu = 0.3)$	60	0.25	-	0.26	$P_L = 175$	-	0.3	10,000	10,000
$E_3 (\mu = 0.5)$	60	0.25	-	0.26	$P_L = 175$	-	0.5	10,000	10,000
$E_3 (\mu = 0.7)$	60	0.25	-	0.26	$P_L = 175$	-	0.7	10,000	10,000

*indicates displacements were applied tangent to the element edges on the upper half of the model. In all other cases displacements are applied normal to the model edges

boundary conditions on the upper and lower model boundaries parallel to the boundary faults (i.e., parallel to x_1) with the assumption that any displacement normal to the boundary faults is continuous along the entire boundary. The lower boundary is fixed (zero displacement boundary conditions) while displacements u_1 and u_3 are prescribed tangential and normal to the upper boundary, respectively (Fig. 5). Because the fault zone extends laterally in the x_1 direction beyond the map, and some cross fractures intersect the x_3 -parallel model boundaries (meaning displacements are expected to be nonuniform along x_3), we avoid prescribing displacements along these boundaries. Instead we prescribe constant normal tractions equivalent to a lithostatic load (P_L) for a burial depth of 7 km, within the range of amphibole geobarometry estimates for emplacement depths of 4–15 km (AGUE and BRIMHALL, 1988). Assuming a gradient of 25 MPa/km and a depth of 7 km we have $P_L = 175$ MPa (Table 1).

In all cases external boundary conditions are applied in two steps. In the first loading stage, we prescribe an isotropic stress state where $\sigma_{11} = \sigma_{33} = P_L$ (Table 1) and no slip occurs anywhere in the model. In the second loading stage we subject the modeled fault zone to a range of combinations of displacements u_1 and u_3 defined by the ratio $r = u_3/u_1$. The choice of r depends on the goal of each set of simulations. For example, in determination of the effective Young's modulus parallel to x_3 , $r = \infty$. For the model confirmation we use $r = 1$. The observation of left- and right-lateral slip on cross fractures suggests that the fault zone has been sheared parallel to and shortened normal to the boundary faults. In each simulation, the frictional strength of the fracture interfaces is characterized by a single constant coefficient of friction μ . We consider a range of possible values for this parameter, and run each loading configuration for $\mu = 0.3$ – 0.7 . Fracture stiffnesses k_N and k_T are assigned constant values of 10,000 GPa/m in all simulations (Table 1). The loading conditions that produce a slip sense and relative magnitudes of slip on model cross fractures similar to geological observations are interpreted to approximate loading conditions on the fault zone *in situ*. Because we cannot constrain the finite deformation path of the fault zone from its initial configuration to the final configuration, we are only concerned with approximating the finite, relative slip magnitudes on the cross fractures.

Figure 6 shows the modeled slip distributions on the cross fractures for $r = 1$ and $\mu = 0.35$ (Table 1). Other values of μ show similar slip distributions with different absolute magnitudes. Under the loading configuration $r = 1$, slip magnitudes are seen to reach a maximum along the faults with the largest measured offsets in the field at locations (i) and (iii). At location (ii) the modeled slip is zero, agreeing with the offset measured in the field at the corresponding location. At location (iv) the modeled slip is right-lateral, consistent with field measurements along the high-angle, antithetic cross fractures. Only at location (v) do the model results disagree significantly with the measured offset in the field, as the offset shown on the map is significantly greater than the modeled slip. This discrepancy is likely due to the fixed lower model boundary. Away from the boundaries, however, the model appears to confirm the response of the fault zone to remotely applied loads.

4.2. Apparent Young's Moduli

We perform uniaxial compression tests on the model fault zone in two configurations to calculate the apparent Young's moduli $E_I = 1/s_{11}'$ and $E_3 = 1/s_{33}'$, where the prime denotes the component of the transformed compliance tensor rotated from the crack-local coordinate system to the global coordinate system. The contraction directions are parallel to x_I (fault parallel) and x_3 (fault normal), respectively. These experimental configurations are illustrated in Figure 7. For E_I (Fig. 7A), the right model boundary is displaced to the left, in the negative x_I direction. The left boundary is frictionless, but is fixed (zero displacement) normal to the boundary. As in the model geometry confirmation experiments, the Young's modulus experiments are initiated in an isotropic stress state, where $\sigma_{11} = \sigma_{33} = P_L$ (Table 1). For the remainder of the experiment, the upper and lower boundaries are subjected to a constant normal traction equal to P_L (Table 1). Such constant stress boundary conditions have been shown to limit internal stress relaxation leading to an accelerated failure process (e.g., BEN-ZION, 2008; LYAKHOVSKY *et al.*, 2001). Because we are not attempting to simulate an entire earthquake cycle, but instead

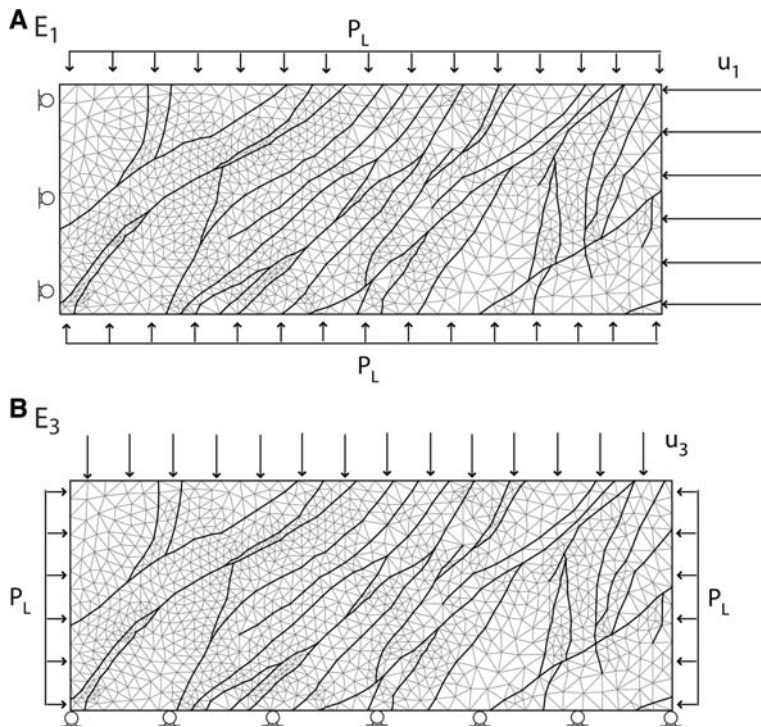


Figure 7

External boundary conditions for apparent Young's modulus uniaxial compression tests. See text for discussion.

mimicking deformation experiments in the laboratory, these boundary conditions should be sufficient. Stresses are calculated from forces recorded at the nodes on the x_1 -parallel boundaries at each loading step, and the average values of these stresses are used in the Young's modulus calculations. The model configuration for the calculation of E_3 (Table 1) is identical to the model configuration for E_1 rotated by 90° (Fig. 7B).

Figure 8 shows the stress-strain curves and apparent effective Young's moduli, E_1 and E_3 ($1/s_{11}'$ and $1/s_{33}'$) calculated for simulations with three different μ values assigned to the damage zone fractures ($\mu = 0.3, 0.5$, and 0.7 ; Table 1). At each loading step, the apparent Young's modulus is calculated as the discrete tangent of the corresponding stress-strain curve. Because the FEM model assumes plane strain deformation, and the plane strain Young's modulus, E_{ps} , is related to the actual Young's modulus, E , by $E = E_{ps}/(1 - \nu^2)$, we multiply the model results by $(1 - \nu^2)$, where ν is the background isotropic value of Poisson's ratio ($\nu = 0.25$). Note that in both cases, E_1 and E_3 initially

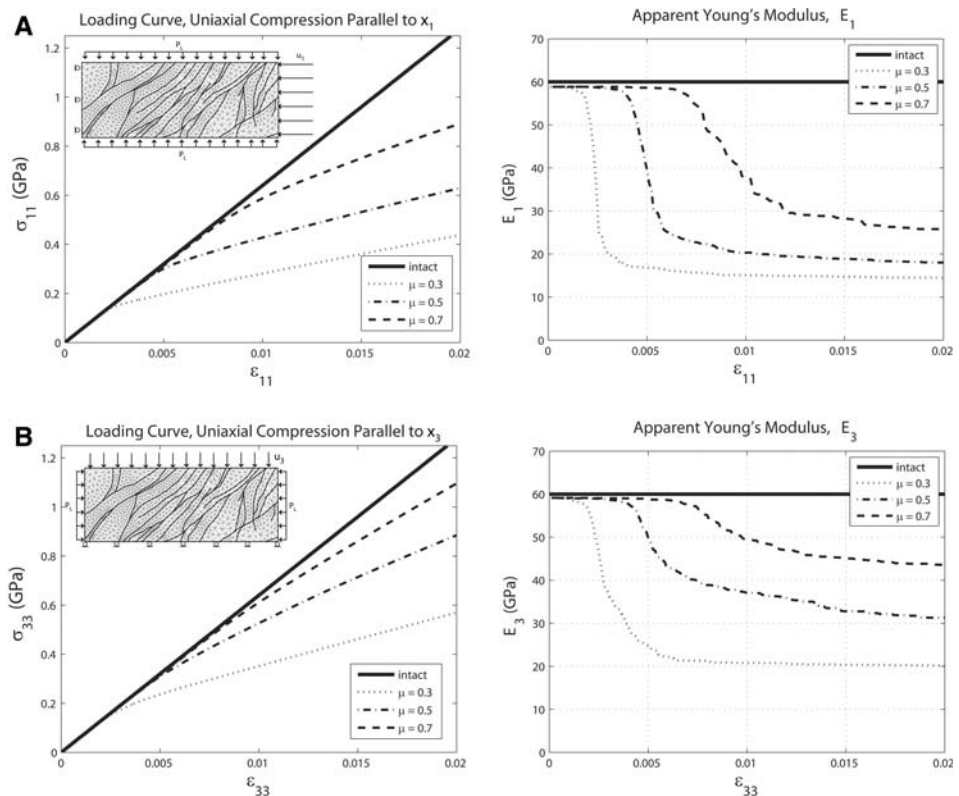


Figure 8

x_3 -parallel Young's modulus (E_3) and x_1 -parallel Young's Modulus (E_1) for three different friction coefficients compared to the background modulus of the intact rock. Upper and lower model boundaries are modelled as frictionless plates. Left plot shows the loading curve and right plot shows the Young's modulus values varying with the corresponding normal strain.

remain constant with increasing strain at a level that is slightly (~ 1 GPa) less than Young's modulus for the intact granodiorite, and then progressively decreases, approaching a residual constant value at ε_{11} or $\varepsilon_{33} = 0.02$, respectively. The constant Young's modulus at the beginning of each experiment is slightly lower than the intact value due to the finite stiffness assigned at the fracture contacts ($k_N = k_T = 10,000$ GPa/m). In all cases, the apparent Young's modulus follows a strain-softening behavior, and achieves the maximum reduction as the normal strain in the shortening direction reaches ε_{11} or $\varepsilon_{33} = 0.02$. Residual values of E_I (Fig. 9A) at $\varepsilon_{11} = 0.02$ are 15 GPa for $\mu = 0.3$, 19 GPa for $\mu = 0.5$, and 26 GPa for $\mu = 0.7$. These apparent Young's moduli represent reductions from the intact value of 75%, 68%, and 57%, respectively. Residual values of E_3 (Fig. 9B) at $\varepsilon_{33} = 0.02$ are 21 GPa for $\mu = 0.3$, for 33 GPa for $\mu = 0.5$, and 46 GPa for $\mu = 0.7$. These apparent Young's moduli represent reductions from the intact value of 65%, 45%, and 23% respectively.

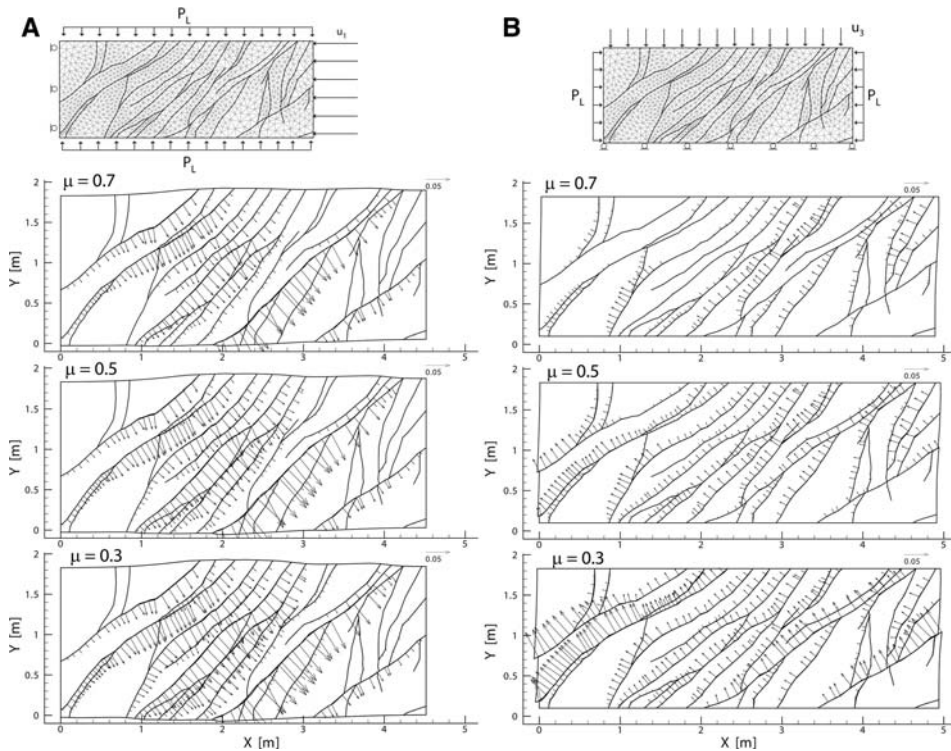


Figure 9

Cumulative slip distribution on cross fractures for each experiment plotted in Figure 8. Slip distributions represent (A) results from the x_1 -parallel apparent Young's modulus (E_I) tests, and (B) results of the x_3 -parallel apparent Young's modulus (E_3) tests. Top, $\mu = 0.7$; middle $\mu = 0.5$; bottom, $\mu = 0.3$. Length of arrows represents slip magnitude. Arrows with negative x component represent left-lateral slip. Larger amounts of slip result in larger reductions in the apparent Young's modulus.

Slip distributions for each simulation are shown in Figure 9, where the lengths of the arrows represent the magnitude of slip, and arrows pointing to the western side of the fractures indicate left-lateral slip. The strain-dependent reduction of effective moduli of fault zone rocks is related to slip on the cross fractures: As a slip patch nucleates and spreads along a fracture the fault zone becomes more compliant (Fig. 9). This is consistent with greater modulus reductions at lesser μ . As strain progresses, however, all of the fractures optimally oriented for slip become active, and the modulus reduces to a constant value. Continued modulus reduction would require the formation of additional fractures. Note that the maximum slip on any of the fractures is on the order of 10 cm.

The fault zone is more compliant under x_1 -parallel loading, and the influence of frictional properties on the bulk compliance is less for this case as seen in the smaller spread between maximum apparent Young's modulus reduction (Fig. 8) and the larger and more extensive slip distributions relative to the case of x_3 -parallel loading (Fig. 9). This difference highlights the anisotropic behavior induced by the damage zone fractures.

4.3. ν , G and K

The numerical simulations focus on the calculation of the effective Young's modulus because the loading configuration is straightforward to implement. The test for the shear modulus, G (defined as $\sigma_{ij} = 2G\epsilon_{ij}$, $i \neq j$), and the bulk modulus, K (defined as $1/3\sigma_{\alpha\alpha} = K\epsilon_{\alpha\alpha}$), is more complicated. The calculation of G requires that the fault zone be loaded in pure shear; however, because the model fracture interfaces have zero tensile strength, any prescribed symmetric shear tractions or displacements along the model boundaries, in the absence of an increasing normal load, would cause the interfaces to separate. The test for K is not difficult to implement, however an isotropic stress state in the model would result in zero frictional slip along the faults (i.e., $K_{\text{damaged}} = K_{\text{intact}}$). This is precisely what happens during the initial loading phase of all of the experiments: loading the fault zone isotropically to P_L returns the intact bulk modulus.

Instead of calculating these moduli directly, we calculate the effective Poisson's ratio for the uniaxial compression tests, and then approximate the corresponding isotropic G and K (Fig. 10). Poisson's ratio is found by calculating normal strain from the difference between the average node displacements on either side of the model in the direction orthogonal to the applied displacement, and substituting these values into $\nu = -\epsilon_{11}/\epsilon_{33}$. The results are shown in Figure 10A for the two compression tests with $\mu = 0.5$. The solid black line is the background isotropic value of $\nu = 0.25$. In the initial loading stages, ν is considerably lower than the isotropic elastic value, again due to stiffness effects of the fractures. As frictional slip commences on the fractures, ν steadily increases to a value of $\nu = 0.3$, at ϵ_{11} or $\epsilon_{33} = 0.004$, at which point the values diverge and that for compression parallel to x_1 approaches $\nu = 0.5$, the value corresponding to an incompressible elastic material.

Substituting the modeled apparent E and ν values into equations (6) and (7), we calculate the effective isotropic G and K for $\mu = 0.5$ (Figs. 10B, C). Because the overall

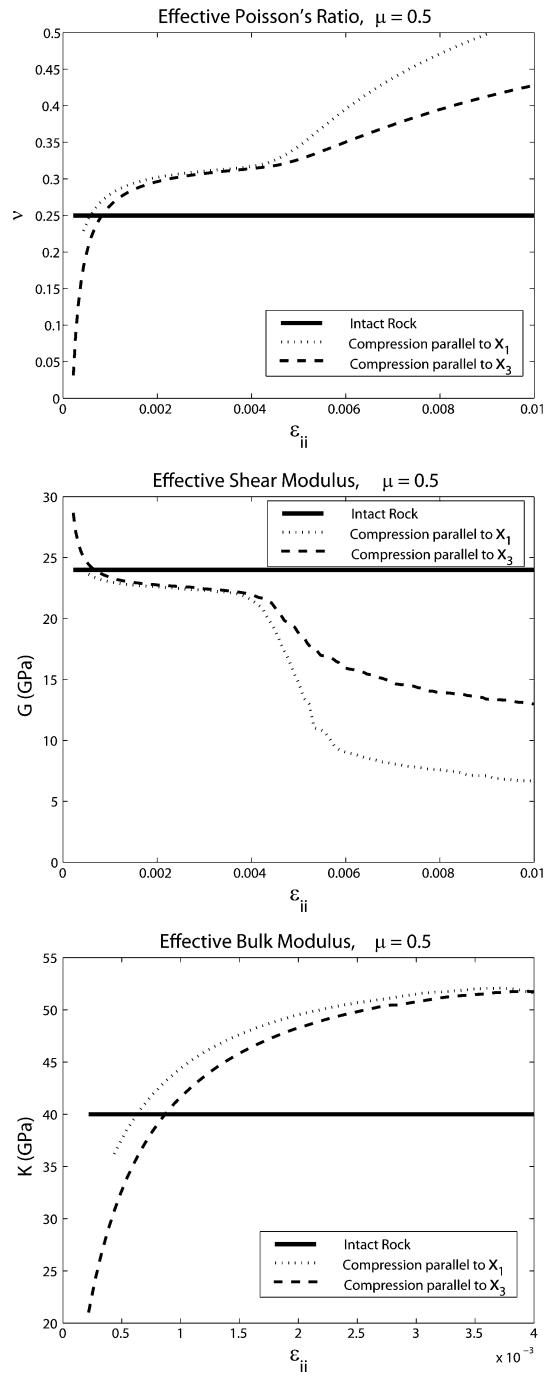


Figure 10
 ν , G , and K calculated from uniaxial compression tests with $\mu = 0.5$.

fault zone response is highly anisotropic and strain-softening (i.e., inelastic), these values are rough approximations, but illustrate the influence of the outcrop-scale fractures on the compliance of the fault zones. Apparent G decreases from an initial state larger than the background isotropic G , and steadily degrades along a trend roughly inverse that of ν . Because the fault zone becomes incompressible at strains of $\varepsilon_{ii} \approx 0.01$, we only show G for values below this threshold. The maximum reduction of $\sim 75\%$ in apparent G (Fig. 10B) relative to G_{intact} (solid line) occurs for the x_1 -parallel compression case (dotted line).

Apparent K is plotted only up to normal strains of ε_{11} or $\varepsilon_{33} \approx 0.004$ (Fig. 10C). Beyond this value apparent K approaches infinity as ν approaches 0.5 (i.e., the fault zone becomes incompressible). Presumably the formation of additional fractures would be encouraged as this incompressible state is reached during deformation of the fault zone *in situ*. Unlike E , ν , and G , the calculated K converges for the two loading conditions with increasing normal strain, as both the fault zone approaches incompressible.

5. Discussion

Both sets of numerical uniaxial compression tests (Fig. 8) show large reductions in effective elastic moduli within the fault zone for normal strains up to 0.02 and total slip on cross-fractures of up to 10 cm. These simulations show that frictional slip on outcrop-scale fractures can result in maximum reductions in the apparent effective Young’s modulus as great as 75%. This is on the order of contrasts imposed by the juxtaposition of rocks of different lithologies. For example, the Young’s modulus of several common rock types is tabulated in Table 2, from BIRCH (1966). This implies that mesoscopic damage zone fracturing can impose a significant material contrast. With more slip and associated damage, this material contrast could become even greater, although hydrothermal mineral precipitation observed in these fault zones (MARTEL *et al.*, 1988; PACHELL and EVANS, 2002) suggests a concurrent healing process that would act to stiffen the fault zone.

This is a significant reduction in effective stiffness for fault zones which were active at depths greater than 4 km (GRIFFITH *et al.*, 2008; MARTEL *et al.*, 1988; SEGALL *et al.*,

Table 2
Some Young’s moduli reported for common rocks, tabulated from BIRCH (1966)

Young’s modulus, E (GPa):		
Rock Type	Dry Modulus	Wet Modulus
Granodiorite, Weston Mass.	60	
Granite, Westerly	40, 71	
Limestone, Solenhofen	55	55
Shale, siltstone	44	19
Halite, Upper Zechstein series	28	

1990). While multiple lines of geophysical (BEN-ZION *et al.*, 2003; FIALKO, 2004) and theoretical (BEN-ZION and SHI, 2005) evidence suggest that significant damage development should be suppressed at such depths, it is clear from field and microscopic evidence that (a) the fault and damage zone fractures remained weaker than the surrounding rocks despite hydrothermal mineral precipitation as evidenced by overprinting fault fabrics and (b) that macroscopic damage zone fractures continued to form throughout the fault zone evolution, as evidenced by the cross-fracture hierarchy and range of fracture filling textures, ranging from undisturbed joint filling to highly comminuted cataclasite. This observation implies that either (i) such localized damage zones might be common even at seismogenic depths, or (ii) this is a special case unique to the Bear Creek faults. In either case, it should be stressed that these damage zones are very thin (0.5–3 m) relative to flower structures (up to several km) and pulverization zones common at shallower depths along crustal scale faults. It is evident that the width of the Bear Creek damage zones was limited by the pre-existing anisotropy, as damage is consistently confined to the region between two subparallel boundary faults. Certainly, the formation of damage could have been encouraged by fault interaction based on the quasi-static analyses of MARTEL and POLLARD (1989) or MARTEL and BOGER (1998). On the other hand, stress drops along these faults have been inferred to be anomalously high, on the order of 100 MPa (GRIFFITH *et al.*, 2009). Such large stress drops could potentially combat the retarding effects of dynamic damage formation due to increasing confining pressure at growing depths (ANDREWS, 2005). In any case, the results of this study suggest that the existence of damage zones of meter-scale thickness should not be precluded along active faults at seismic depths, and that these damage zones may significantly reduce the rock stiffness adjacent to the principal slip zone.

The numerical simulations conducted in this study also show that the frictional slip on outcrop-scale fractures leads to a bulk nonlinear strain-softening response of the damage zone. This implies that the effective stiffness could vary dramatically throughout a single rupture event, and throughout the evolution of the fault zone, even in the short term (i.e., at strains much less than 2%). While it is clear that the cross fractures formed as opening-mode features and many of the cross fractures slipped on multiple occasions during the evolution of the fault zone, the timing and rate of deformation are not known. The cross fractures are compositionally and microstructurally similar to the boundary faults, however this does not provide sufficient information to ascertain whether or not they slipped simultaneously with rupture events on the boundary faults. Also, because the cross fractures do not contain pseudotachylite, it is difficult to assess the rate at which these fractures slipped.

These numerical simulations are instructive because they allow for the relaxation of some of the key assumptions of the analytical models. Compared to the micromechanical models (Appendix A), there is no maximum fracture density requirement, and compared to the stiff parallel joint model of AMADEI and SAVAGE (1993) the deformation of the fractures need not be entirely elastic. Assumptions common to all of the analytical models are that the fractures are parallel, do not intersect, and are uniformly distributed

throughout the entire fractured rock body. Clearly none of these are valid assumptions based on mapping of the fault zone fractures. The stiff parallel joint model may be the most appropriate model for a mesoscopically fractured damage zone, however this model is difficult to constrain for rocks *in situ*. Even if it were reasonable to assume that the fractures deformed elastically, deformability of the fractures in the stiff parallel joint model is based on the fracture stiffness. Because fracture stiffness is strongly dependent on normal load (e.g., YOSHIOKA and SCHOLZ, 1989a, 1989b) and may vary by several orders of magnitude both spatially and temporally, the fracture stiffness may change appreciably during a transient slip event and laterally along each fracture depending on the fracture filling and roughness of the fracture faces. Instead, the numerical approach accurately represents the mapped geometry of the fault zone and faults and fractures interact and slip when their Coulomb strength is exceeded. The contact problem is more easily constrained for the numerical experiments, as friction coefficients for fault rocks are independent of the normal load.

There are a number of limitations to the current study, some of which could be improved with future work: (1) First, we assume that the frictional properties of the faults are constant throughout a deformation cycle. This is a simplification of the real system as frictional strength is expected to change during and between slip events. (2) We do not include effects of fluid pressure and transport. It is apparent that hydrous conditions persisted throughout the fault activity. The presence of fluids along these faults would add contrasting effects of weakening the fractures by lowering the effective normal stress and increasing the peak strength of the fractures by enhancing the healing process between slip events. (3) The rocks between the modeled fractures are assumed to deform elastically, which fails to represent the observed pattern of increasing fracture density with fault zone evolution. A more realistic approach for future studies would be to represent the faults with a plastic rheology, or the nonlinear damage rheology of LYAKHOVSKY *et al.* (1997). (4) Finally, these results are scale-sensitive. While the bulk response of the fault zone to external loads is significantly different than for the intact case, the fault zone experiences large internal deformation gradients. Therefore the expected local stiffness is expected to vary considerably throughout the fault zone.

6. Conclusions

We combine detailed mapping and microstructural analysis of fault zones in the Bear Creek drainage of the central Sierra Nevada with numerical Finite-Element methods to estimate the contribution of outcrop-scale fractures to the effective stiffness of the fault rocks. The Bear Creek fault zones were active at seismogenic (4–15 km) depths and localize mesoscopic off-fault damage into thin (0.5–3 m) tabular zones between two subparallel boundary faults, producing a fracture-induced material contrast across the boundary faults. Frictional slip on the mesoscopic damage zone fractures results in a bulk strain-softening response of the fault damage zone, thus the effective moduli are expected

to vary during individual slip events and during the longer term evolution of the fault zones. The material within the boundary faults can be as much as 75% softer than the adjacent undamaged granodiorite, even within juvenile fault zones ($\sim 8\text{--}10$ m total offset). For larger, more mature fault zones this material contrast could be significantly greater, even at seismogenic depths.

Acknowledgements

Thoughtful reviews by Y. Ben-Zion, R. Weinberger, and an anonymous reviewer greatly improved this manuscript. G. Di Toro, G. Pennacchioni, and S. Nielsen assisted in field work, and the National Forest Service graciously provided sampling permission in the John Muir National Wilderness. This work was supported financially by the Rock Fracture Project, Stanford University, National Science Foundation Grant No. CMG-0417521 (Collaborations in Mathematical Geosciences), and the U.S. Geological Survey (USGS), Department of Interior, under USGS award number 08HQGR0010. The views and conclusions contained in this document are those of the authors and should not be interpreted as necessarily representing the official policies, either expressed or implied, of the U.S. Government.

Appendix A: Analytical Models

Analytical effective medium models present an efficient means for calculating effective elastic properties of fractured rock masses given an estimate of the nondimensional spatial density of fractures, and can be used to invert for fracture density given seismic velocities for the fractured rock. A more recent formulation replaces the fracture density parameter with a damage variable which allows the modeled cracks to contract or dilate during deformation (LYAKHOVSKY *et al.*, 1997). An attractive feature of these models is that given some basic assumptions about the anisotropy of the fractured medium (e.g., that it is transversely anisotropic), one can define the complete anisotropic compliance or stiffness tensor. Here we evaluate the applicability of several analytical effective medium models for describing the bulk response of the BJFZ.

Most effective medium theories for cracked solids are based on micromechanics (e.g., WALSH, 1965a, b; KACHANOV, 1992; JAEGER *et al.*, 2007 and references therein), and consist of several classes, including (i) zero interaction; (ii) self-consistent; and (iii) wave scattering. The zero interaction models treat each fracture as if it were isolated as a single fracture in an otherwise undamaged material, and then sums the effect of all of the cracks within the body. In the self-consistent models (e.g., O'CONNELL and BUDIANSKY, 1974), each crack is treated similar to the zero interaction models, except that the effect of each crack is added to the overall moduli of the cracked material in an iterative process, so that the effect of each successive fracture is calculated against an increasingly lower

background modulus. The first two general formulations, then, provide lower and upper bounds on the effects of the cracks on the effective elastic moduli, respectively. A third class of effective medium theories (e.g., HUDSON, 1980) approaches the problem using scattering theory analysis of the mean field in an isotropic elastic solid embedded with thin cracks. Like the self-consistent method, this approach also takes into account interaction between cracks.

A common feature of most micromechanical models described above is that the fractures are represented by a single spatial parameter, the fracture density, Γ , represented by (e.g. WALSH, 1965):

$$\Gamma_{3D} = \frac{1}{V} \sum_{i=1}^N a_i^3, \quad \text{and} \quad \Gamma_{2D} = \frac{1}{A} \sum_{i=1}^N a_i^2, \quad (\text{A1})$$

where N is the number of fractures, a is the fracture half-radius or half-length, V is the total rock volume, A is the total rock area, and subscripts 3-D and 2-D refer to the three- and two-dimensional forms of the fracture density, respectively. All of the models yield similar results for fracture densities less than $\sim \Gamma_{3D} \approx 0.2$ but disagree at higher densities (KACHANOV, 1992; JAEGER *et al.*, 2007). Whereas these micromechanical models are sufficient for describing overall effects of microcracks in sparsely fractured rocks, their limitations make them inadequate for descriptions of many natural mesoscopic and macroscopic fracture systems, which typically have fracture densities on the order of $\Gamma_{2D} \approx 1$ to 2 (RENSHAW, 1997). Using equation (A1) above, the digitized BJFZ fracture map yields a fracture density of $\Gamma_{2D} = 1.36$ (Fig. A1); therefore we must select an effective medium model which allows higher fracture densities.

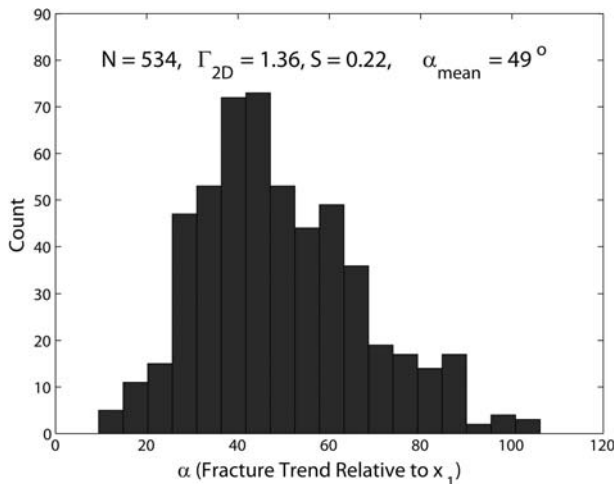


Figure A1

Fracture orientation (α) relative to the positive x_1 axis. N is the number of measured segments, S is the calculated spacing in meters, α_{mean} is the mean fracture orientation, and Γ_{2D} is the two-dimensional fracture density.

A different approach accounts for nonlinear elastic behavior of rocks due to opening and closing of cracks (e.g., ZOBACK and BYERLEE, 1975; WEINBERGER *et al.*, 1994) by adding a second-order term in the elastic potential of a Hookean solid (LYAKHOVSKY *et al.*, 1997b). Damage mechanics has been shown to successfully match experimental rock deformation for arbitrary loading paths (e.g., HAMIEL *et al.*, 2006). This approach does not suffer from exactly the same limitation as the methods described above, as it uses a scalar damage variable which depends on the change in the elastic strain energy potential during deformation (e.g., LYAKHOVSKY *et al.*, 1997a). However, this approach is difficult to apply to the present case of estimating the overall response of macroscopic frictional fractures, as it estimates stiffness changes independent of any previous structural features. Therefore there is no statistical way to represent the macroscopic damage zone fractures in the model.

Still another approach to estimating the elastic moduli of fractured rocks is to treat the fractures as evenly distributed and parallel with characteristic normal and shear stiffness (AMADEI and SAVAGE, 1993). In this approach, the spatial distribution is characterized by the fracture spacing, S , rather than the fracture density, Γ . Fractures are idealized with negligible thickness and infinite length, and their mechanical behavior is characterized by a normal stiffness k_n and shear stiffness k_s . The method is independent of fracture density and subscripts n and s are chosen here to differentiate these stiffnesses from the stiffnesses k_N and k_T used as regularization parameters in the numerical models. For one set of fractures perpendicular to the positive x_3^c axis the compliances are:

$$\begin{aligned} s_{11} &= s_{22} = \frac{1}{E}, \\ s_{33} &= \frac{1}{E} + \frac{1}{k_n S}, \\ s_{44} &= s_{55} = \frac{1}{G} + \frac{1}{k_s S}, \\ s_{66} &= \frac{1}{G}, \\ c_{12} &= c_{13} = -\frac{\nu}{E}. \end{aligned} \tag{A2}$$

We idealize the fractures of the BJFZ (Fig. 3) as a set of parallel joints with spacing S and orientation α relative to the positive x_1 direction. In order to estimate values of these parameters, we take advantage of the digitized maps produced during the finite-element mesh generation. The fractures are divided into short subequal length segments, where the length of each segment equals the corresponding segment lengths in the Finite-Element grid (Fig. 5). The orientations of all of the fracture segments relative to the positive x_1 axis are plotted in Figure A1. There is one dominant fracture orientation at $\alpha \approx 49^\circ$ with a spread of one standard deviation = 16° . We calculate the fracture spacing using the area method described by WU and POLLARD (1995), yielding $S \approx 0.22$ m. Using these parameters, a large range of effective moduli can be calculated

depending on the choice of k_n and k_s . Because fracture stiffness may vary over several orders of magnitude and is highly sensitive to the normal traction acting on the fracture (e.g., WORTHINGTON and LUBBE, 2007; YOSHIOKA and SCHOLZ, 1989a, b) we attempt to use the numerical results to constrain these parameters for the BJFZ.

Using the effective medium model, the compliances are calculated in the crack-local reference frame (Fig. 2) using eqns. (2) and (A2). We calculate the apparent Young's moduli parallel to the x_1 and x_3 axes in the global reference frame in the numerical experiments. These correspond to $E_3 = 1/s_{33}'$ and $E_1 = 1/s_{11}'$ in the compliance matrix transformed into global reference frame (S') by rotating around the mean fracture orientation angle $\alpha = 49^\circ$ using the Bond transformation matrix N (e.g., MAVKO *et al.*, 1998):

$$S'(k_n, k_s) = NS(k_n, k_s)N^T. \quad (\text{A3})$$

In equation (A2), s_{33} is a function of E , S , and k_n , while s_{11} is only a function of E . However, through the rotational transformation (equation (A3)) from crack-local to global reference frame s_{11}' and s_{33}' both become functions of k_n and k_s as follows. By defining the two strain and stress vectors as:

$$\begin{aligned} \varepsilon_1 &= S'(k_n, k_s)\sigma_1; & \sigma_1 &= [1 \quad 0 \quad 0 \quad 0 \quad 0 \quad 0]^T, \\ \varepsilon_3 &= S'(k_n, k_s)\sigma_3; & \sigma_3 &= [0 \quad 0 \quad 1 \quad 0 \quad 0 \quad 0]^T, \end{aligned} \quad (\text{A4})$$

one can calculate the x_1 and x_3 -parallel apparent Young's moduli. The problem of solving for the crack stiffnesses can be reduced to two equations in two unknowns:

$$E_1 = \frac{\varepsilon_1}{\sigma_1} = \frac{1}{s_{11}'(k_n, k_s)} \quad \text{and} \quad E_3 = \frac{\varepsilon_3}{\sigma_3} = \frac{1}{s_{33}'(k_n, k_s)}. \quad (\text{A5})$$

The expressions for s_{11}' and s_{33}' are:

$$\begin{aligned} s_{11}' &= \frac{1}{E} + \frac{\sin^4 \alpha}{k_n S} + \frac{\sin^2 2\alpha}{4k_s S}, \\ s_{33}' &= \frac{1}{E} + \frac{\cos^4 \alpha}{k_n S} + \frac{\sin^2 2\alpha}{4k_s S}. \end{aligned} \quad (\text{A6})$$

The other components of the transformed compliance matrix can be found using equations (A2) and (A3) and are written down in AMADEI and SAVAGE (1993). Finally, solving these equations for k_n and k_s yields:

$$\begin{aligned} k_n &= \frac{-1 + 2 \cos^2 \alpha}{S(s_{33}' - s_{11}')}, \\ k_s &= -\frac{E \sin^2 2\alpha (\sin^4 \alpha - \cos^4 \alpha)}{4S([1 - Es_{33}'] \sin^4 \alpha - [1 - Es_{11}'] \cos^4 \alpha)}. \end{aligned} \quad (\text{A7})$$

Substituting these values of k_n and k_s constrained by the numerical calculations of the apparent Young's moduli into equation (A2), one can define the complete transversely

anisotropic compliance matrix. As an example, substituting values of $E = 60$ GPa and $\alpha = 49^\circ$, as well as $E_I = 20$ GPa and $E_3 = 37$ GPa from the uniaxial compression tests for $\mu = 0.5$ at ε_{11} or $\varepsilon_{33} = 0.01$ into equation (A7) yields crack stiffnesses of $k_n = 28$ GPa/m and $k_s = -55$ GPa/m. Clearly, negative crack stiffness is not valid. Although this procedure is valid for a very small range of results at extremely small strains (ε_{11} or $\varepsilon_{33} \ll 0.005$), this analytical model and the numerical experiments are not compatible.

There are several sources of this incompatibility. The most obvious are the constitutive assumptions built into the models. The analytical model assumes that the fractures deform only elastically based on k_n and k_s . Under this assumption, the largest reduction in the apparent Young's modulus occurs when the fractures are orthogonal to the direction of maximum compression. Under this configuration the classical Coulomb friction model predicts zero sliding, thus no reduction in the Young's modulus. A second source of incompatibility is the scale of the problem. The BJFZ, and, for that matter, all of the fault zones in the Bear Creek area are tabular in shape and much longer (in the x_1 direction) than they are wide (in the x_3 direction). This and a nonuniform fracture distribution lead to large stress and strain variations across them during the numerical uniaxial tests. An assumption of the analytical model is that the rock mass is large enough to contain numerous fractures, yet small enough to make stress and strain gradients within it negligible. Clearly this criterion is not satisfied. Finally, while the cross fractures of the BJFZ have a preferred orientation (Fig. A1), they anastomose and intersect such that there is a large spread in fracture orientations across the fault zone, and the fractures are not infinite in length. Thus the assumption of an array of long parallel fractures is an insufficient idealization for the fault zone.

Appendix B: Numerical Model

Rock masses are disordered discontinuous media in which the main hydraulic and mechanical features are the discontinuities (BIENIAWSKI, 1978). Consequently, a very important aspect of modeling rock masses is the appropriate representation of these discontinuities, either as individual entities (explicitly through interfaces) or as a homogenized system (implicitly as diffuse discontinuities, i.e., continuum approach). The suitability of these models depends on the problem scale relative to the fracture density and on the configuration of the discontinuities. Continuum approaches should be used for rock masses with no discontinuities (intact rock) or with many of them (equivalent continuum rock mass), where the equivalent properties of the latter can be established through a homogenization process or through empirical relations (e.g., BIENIAWSKI, 1978; HOEK and DIEDERICH, 2006; SONMEZ *et al.*, 2006).

To adequately capture the mechanics of the fault damage zone, we implement a model that explicitly captures discontinuous displacement fields. Here we develop a model based upon continuum mechanics and frictional contacts in which the coupling between the deformation of both the rock matrix and the rock discontinuities is

realistically accounted for. A key goal of this study is to model the fracture evolution accounting for frictional sliding. A constitutive model for geologic interfaces considering unilateral contact and inelastic relative motion is presented and implemented into a finite-element code following SANZ (2008).

With contact mechanics it is possible to capture a normal discontinuity (gap), a tangential discontinuity (slip), or no discontinuity (stick or bonded) along a pre-defined interface. A critical aspect of the implementation is the choice of method to convert the variational inequality of a contact constraint into an equality suitable for the finite element framework. This implementation applies the penalty method to impose the contact constraints and a regularized friction law to simulate the mechanical response of the interfaces (LAURSEN, 2002; WRIGGERS, 2002). The numerical integration of these path-dependent interface models is performed by a return mapping algorithm similar to a non-associative plasticity model (WRIGGERS, 2002).

Contact Kinematics and Traction Measures

The contact condition is defined in the initial (i.e., undeformed) configuration via a minimum distance problem or closest point projection (e.g., LAURSEN, 2002; WRIGGERS, 2002) such that every point \mathbf{X}^1 on a contact surface can be related to a point \mathbf{X}^2 on the other contact surface. The relative displacement between these two contact points is defined as

$$\mathbf{g} = \mathbf{u}(\mathbf{X}^2) - \mathbf{u}(\mathbf{X}^1) = \mathbf{u}^2 - \mathbf{u}^1, \quad (\text{B1})$$

where \mathbf{u}^1 and \mathbf{u}^2 are the displacements of the material points \mathbf{X}^1 and \mathbf{X}^2 , respectively.

The relative displacement \mathbf{g} can be additively decomposed into a normal part \mathbf{g}_N and a tangential part \mathbf{g}_T as follows

$$\mathbf{g} = \mathbf{g}_N + \mathbf{g}_T, \quad (\text{B2})$$

where

$$\mathbf{g}_N = (\mathbf{n}_N \otimes \mathbf{n}_N) \cdot \mathbf{g}; \quad \mathbf{g}_T = \mathbf{g} - \mathbf{g}_N = (\mathbf{1} - \mathbf{n}_N \otimes \mathbf{n}_N) \cdot \mathbf{g}, \quad (\text{B3})$$

where \mathbf{n}_N is the unit outward normal to the contact surface, $\mathbf{1}$ is the second-order identity tensor, and the symbol \otimes denotes a juxtaposition, e.g., $(\mathbf{a} \otimes \mathbf{b})_{ij} = a_i b_j$.

Let the contact traction \mathbf{t} acting on the interface be decomposed into a normal traction \mathbf{t}_N and a tangential traction \mathbf{t}_T as follows

$$\mathbf{t} = \mathbf{t}_N + \mathbf{t}_T = t_N \mathbf{n}_N + t_T \mathbf{n}_T = \sum_{A=1}^2 t_A \mathbf{n}^{(A)}, \quad (\text{B4})$$

where $t_N = \mathbf{t} \cdot \mathbf{n}_N$ is the contact pressure (negative for compression), $t_T = \|\mathbf{t}_T\|$ and $\mathbf{n}_T = \mathbf{t}_T / \|\mathbf{t}_T\|$ is a unit vector tangent to the surface in the direction of $\mathbf{t}_T = \mathbf{t} \cdot (\mathbf{1} - \mathbf{n}_N \otimes \mathbf{n}_N)$. The component $A = 1$ corresponds to the direction \mathbf{n}_N perpendicular to the interface, and the component $A = 2$ corresponds to the tangential direction \mathbf{n}_T .

Interface Elastic Model

Analogous to plasticity theory, the total relative displacement \mathbf{g} and relative velocity $\dot{\mathbf{g}}$ are decomposed into an elastic part and a plastic part

$$\mathbf{g} = \mathbf{g}^e + \mathbf{g}^p \Leftrightarrow \dot{\mathbf{g}} = \dot{\mathbf{g}}^e + \dot{\mathbf{g}}^p. \quad (\text{B5})$$

The relationship between the traction \mathbf{t} and the elastic relative displacement \mathbf{g} follows Hooke's law and can be written in rate form as

$$\dot{\mathbf{t}} = \mathbf{C}^e \cdot \dot{\mathbf{g}}^e \Leftrightarrow \begin{bmatrix} \dot{t}_N \\ \dot{t}_T \end{bmatrix} = \begin{bmatrix} k_n & 0 \\ 0 & k_T \end{bmatrix} \begin{bmatrix} \dot{g}_N^e \\ \dot{g}_T^e \end{bmatrix}, \quad (\text{B6})$$

where \dot{g}_N^e and \dot{g}_T^e are the normal and tangential elastic components of the relative velocity between the contacting surfaces, and

$$\mathbf{C}^e = k_N(\mathbf{n}_N \otimes \mathbf{n}_N) + k_T(\mathbf{n}_T \otimes \mathbf{n}_T), \quad (\text{B7})$$

a second-order tensor, is the elastic stiffness of the interface. In this work, it is assumed that Eq. (B7) is linear, and the components of the elastic stiffness $\mathbf{C}_{AB}^e = \partial t_A / \partial g_B^e$ are constants. However, there may be applications in which the use of stress dependent \mathbf{C}_{AB}^e are desirable such as in problems involving rock joints subject to large variations of compressive stress in which it is known that k_N and k_T are monotonically increasing functions of increasing compressive stress (e.g., YOSHIOKA and SCHOLZ, 1989a, b). To provide symmetric normal and tangential stress changes for positive and negative changes in the relative normal and tangential displacement, respectively, the off diagonal components of \mathbf{C}^e are zero. The tangential and normal elastic stiffness, $k_T = \partial t_T / \partial g_T^e$ and $k_N = \partial t_N / \partial g_N^e$, are measurable and numerous values have been reported in the literature (e.g., MAHTAB, 1969; GOODMAN *et al.*, 1972; ROSSO, 1976; BELYTCHKO *et al.*, 1984). In the numerical simulations large values for the tangential stiffness used to approximate the rigid-plastic behavior of the classical Coulomb friction law, and a high value of the normal elastic stiffness were used to avoid unrealistic interpenetration between contacting surfaces (Table 1).

Interface Frictional Model

The frictional behavior of the interface is represented by the Coulomb law. Similarly to a yield function in elastoplasticity the function $\Phi(\mathbf{t}_N, t_T) = 0$ (Fig. B1), a conical surface in the (\mathbf{t}_N, t_T) stress space, defines the onset of irreversible relative motion as

$$\Phi(\mathbf{t}_N, t_T) = \|\mathbf{t}_T\| - (c - \mu t_T) \leq 0, \quad (\text{B8})$$

where the shear strength of the interface is defined by the coefficient of friction μ .

The classical Coulomb friction law has an indeterminate, or multi-valued, structure when viewed as a law relating tangential stresses to slip. To avoid the non-differentiability of the friction law at the onset of sliding (i.e., zero relative tangential displacement), we use a regularized version of the stick-slip behavior (Fig. B2).

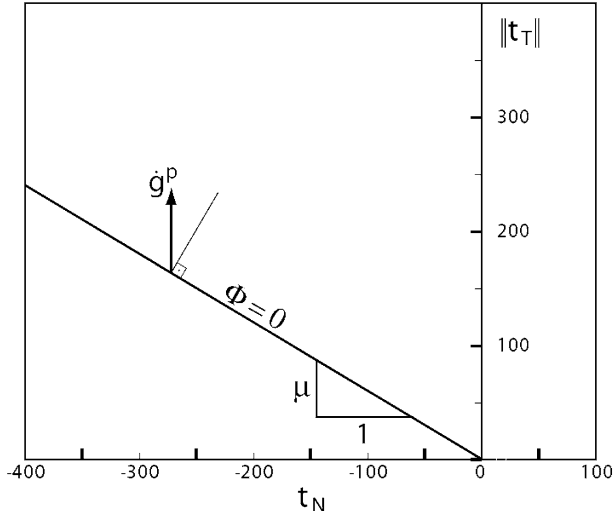


Figure B1

Coulomb slip criterion plotted on graph of tangential versus normal traction. The tangential evolution of the inelastic relative motion (parallel to the vertical axis) illustrates the non-associative nature of the classical Coulomb friction law.

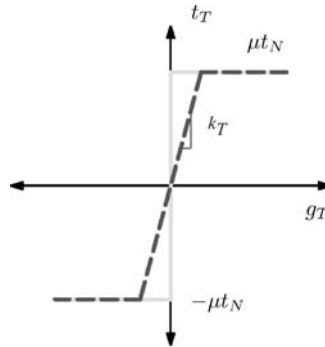


Figure B2

Schematic representation of the regularization of the Coulomb friction law. Dashed line represents the regularization of the exact Coulomb rigid-slip formulation (represented by a gray solid line).

The evolution of the inelastic component of the relative displacement \mathbf{g}^p is described through a non-associative flow rule as

$$\dot{\mathbf{g}}^p = \dot{\lambda} \mathbf{n}_T, \quad (\text{B9})$$

where as in plasticity $\dot{\lambda}$ is the non-negative plastic multiplier.

When an interface undergoes inelastic relative motion (i.e., frictional slip) the second-order interface tangent stiffness takes the following form

$$\mathbf{C}^{ep} = k_N(\mathbf{n}_N \otimes \mathbf{n}_N) - \mu k_N(\mathbf{n}_T \otimes \mathbf{n}_N). \quad (\text{B10})$$

The derivation of the interface tangent stiffness and details regarding the numerical implementation can be found in SANZ (2008).

REFERENCES

- AGUE, J. J. and BRIMHALL, G. H. (1988), *Magmatic arc asymmetry and distribution of anomalous plutonic belts in the batholiths of California: Effects of assimilation, crustal thickness, and depth of crystallization*. Geol. Soc. Am. Bull. 100, 912–927.
- AMADEI, B. and SAVAGE, W. Z. *Effects of joints on rock mass strength and deformability*. In *Comprehensive Rock Engineering*, Vol. I (ed. J. A. HUDSON), pp. 331–365 (Pergamon Press 1993).
- AMPUERO, J.-P. and BEN-ZION, Y. (2008) *Cracks, pulses and macroscopic asymmetry of dynamic rupture on a bimaterial interface with velocity-weakening friction*, Geophys. J. Int. 173, 674–692, doi: [10.1111/j.1365-246X.2008.03736.x](https://doi.org/10.1111/j.1365-246X.2008.03736.x).
- ANDREWS, D. J. and BEN-ZION, Y. (1997), *Wrinkle-like slip pulse on a fault between different materials*, J. Geophys. Res. 102(B1), 553–571.
- ANDREWS, D. J. (2005), *Rupture dynamics with energy loss outside the slip zone*, J. Geophys. Res. 110, doi: [10.1029/2004JB003191](https://doi.org/10.1029/2004JB003191).
- ANDREWS, D. J. and HARRIS, R. A. (2005), *The wrinkle-like slip pulse is not important in earthquake dynamics*, Geophys. Res. Lett. 32, doi: [10.1029/2005GL023996](https://doi.org/10.1029/2005GL023996).
- BELYTSCHKO, T., PLESHA, M. E., and DOWDING, C. H. (1984) *A computer method for stability analysis of caverns in jointed rock*, Int. J. Numer. Anal. Methods Geomech. 8, 473–492.
- BEN-ZION, Y. (2006a), *Comment on “The wrinkle-like slip pulse is not important in earthquake dynamics” by D. J. ANDREWS and R. A. HARRIS*, Geophys. Res. Lett. 33, L06310, doi: [10.1029/2005GL025372](https://doi.org/10.1029/2005GL025372).
- BEN-ZION, Y., (2006b), *A comment on “Material contrast does not predict earthquake rupture propagation direction” by R. A. HARRIS and S. M. DAY*, Geophys. Res. Lett. 33, L13310, doi: [10.1029/2005GL025652](https://doi.org/10.1029/2005GL025652).
- BEN-ZION, Y. (2008), *Collective behavior of earthquakes and faults: Continuum-discrete transitions, progressive evolutionary changes and different dynamic regimes*, Rev. Geophys. 46, doi: [10.1029/2008rg000260](https://doi.org/10.1029/2008rg000260).
- BEN-ZION, Y., PENG, Z., OKAYA, D., SEEGER, L., ARMBRUSTER, J. G., OZER, N., MICHAEL, A. J., BARIS, S. and AKTAR, M. (2003), *A shallow fault zone structure illuminated by trapped waves in the Karadere-Duzce branch of the North Anatolian Fault, western Turkey*, Geophys. J. Int. 152, 699–717.
- BEN-ZION, Y. and SAMMIS, C. G. (2003), *Characterization of fault zones*, Pure Appl. Geophys. 160, 677–715.
- BEN-ZION, Y. and SHI, Z. (2005), *Dynamic rupture on a material interface with spontaneous generation of plastic strain in the bulk*, Earth Planet. Sci. Lett. 236, 486–496, doi: [10.1016/j.epsl.2005.03.025](https://doi.org/10.1016/j.epsl.2005.03.025).
- BERGBAUER, S. and MARTEL, S. J. (1999), *Formation of joints in cooling plutons*, J. Struct. Geol. 21(7), 821–835.
- BIEGEL, R. L., SAMMIS, C. G., and ROSAKIS, A. J. (2008), *An experimental study of the effect of off-fault damage on the velocity of a slip pulse*, J. Geophys. Res. 113, doi: [10.1029/2007JB005234](https://doi.org/10.1029/2007JB005234).
- BIENIAWSKI, Z. T. (1978), *Determining rock mass deformability: Experience from case histories*, Int. J. Rock Mech. and Min. Sci. and Geomech. Abs. 15, 237–248.
- BIRCH, F. (1966), *Compressibility: Elastic constants*. In *Handbook of Physical Constants*, Vol. 97 (ed. S. P. CLARK), pp. 97–173. Geological Society of America, Memoir.
- BORJA, R. I., SAMA, K. M., and SANZ, P. F. (2003), *On the numerical integration of three-invariant elastoplastic constitutive models*, Comp. Meth. Appl. Mech. Eng. 192, 1227–1258.
- CHESTER, F. M., EVANS, J. P., and BIEGEL, R. L. (1993), *Internal structure and weakening mechanisms of the San Andreas fault*, J. Geophys. Res. 98(B1), 771–786.
- CHESTER, F. M. and CHESTER, J. S. (1998), *Ultracataclasite structure and friction processes of the San Andreas fault*, Tectonophysics 295, 195–221.
- CHESTER, F. M., CHESTER, J. S., KIRSCHNER, D. L., SCHULTZ, S. E., and EVANS, J. P. *Structure of large-displacement, strike-slip fault zones in the brittle continental crust*. In *Rheology and Deformation in the*

- Lithosphere at Continental Margins* (ed. G. D. KARNER, B. TAYLOR, N. W. DRISCOLL, and D. L. KOHLSTEDT) (Columbia University Press 2004).
- CROOK, A. J. L., OWEN, D. R. L., WILSON, S. M., and YU, J. G. (2006), *Benchmarks for the evolution of shear localisation with large relative sliding in frictional materials*, *Comp. Meth. Appl. Mech. Eng.* 195, 4991–5010.
- CROOK, A. J. L., WILSON, S. M., YU, J. G., and OWEN, D. R. L. (2006), *Predictive modeling of structure evolution in sandbox experiments*, *J. Struct. Geol.* 17, 409–421.
- DAVATZES, N. C. and AYDIN, A. (2003), *Overprinting faulting mechanisms in high porosity sandstones of SE Utah*, *J. Struct. Geol.* 25, 1795–1813.
- DOR, O., ROCKWELL, T. K., and BEN-ZION, Y. (2006), *Geological observations of damage asymmetry in the structure of the San Jacinto, San Andreas and Punchbowl faults in southern California: A possible indicator for preferred rupture propagation direction*, *Pure Appl. Geophys.* 163, 301–349.
- FAULKNER, D. R., MITCHELL, T. M., HEALY, D., and HEAP, M. J. (2006), *Slip on “weak” faults by the rotation of regional stress in the fracture damage zone*, *Nature* 444, doi:[10.1038/nature05353](https://doi.org/10.1038/nature05353).
- FIALKO, Y. (2004), *Probing the mechanical properties of seismically active crust with space geodesy: Study of the co-seismic deformation due to the 1992 M_w 7.3 Landers (southern California) earthquake*, *J. Geophys. Res.* 109, doi:[10.1029/2003JB002756](https://doi.org/10.1029/2003JB002756).
- FINZI, Y., HEARN, E. H., BEN-ZION, Y., and LYAKHOVSKY, V. (2009), *Structural properties and deformation patterns of evolving strike-slip faults: Numerical simulations incorporating damage rheology*, *Pure Appl. Geophys.* 166.
- GERCEK, H. (2007), *Poisson's ratio values for rock*, *Int. J. Rock Mech. Min. Sci.* 44, 1–13.
- GOODMAN, R. E., HEUZE, F. E., and OHNISHI, Y. (1972), *Research on strength-deformability water pressure relationship for faults in direct shear*. Final Report, ARPA Contract H0210020, Univ of Cal., Berkeley.
- GRIFFITH, W. A., DI TORO, G., PENNACCHIONI, G., and POLLARD, D. D. (2008), *Thin pseudotachylytes in faults of the Mt. Abbot quadrangle, Sierra Nevada: Physical Constraints for Small Seismic Slip Events*, *J. Struct. Geol.* 30, 1086–1094.
- GRIFFITH, W. A., DI TORO, G., PENNACCHIONI, G., POLLARD, D. D., and NIELSEN, S. (2009), *Static stress drop associated with brittle slip events on exhumed faults*, *J. Geophys. Res.* 114, B02402, doi:[10.1029/2008JB005879](https://doi.org/10.1029/2008JB005879).
- HAMIEL, Y., KATZ, O., LYAKHOVSKY, V., RECHES, Z., and FIALKO, Y. (2006), *Stable and unstable damage evolution in rocks with implications to fracturing of granite*, *Geophys. J. Int.*, doi: [10.1111/j.1365-246X.2006.03126](https://doi.org/10.1111/j.1365-246X.2006.03126).
- HAMIEL, Y., LYAKHOVSKY, V., STANCHITS, S., DRESEN, G., and BEN-ZION, Y. (2008), *Brittle deformation and damage-induced seismic wave anisotropy in rocks*, *Geophys. J. Int.*, in review, 2008.
- HARRIS, R. A. and DAY, S. M. (2005), *Material contrast does not predict earthquake rupture propagation direction*, *Geophys. Res. Lett.* 32, doi:[10.1029/2005GL023941](https://doi.org/10.1029/2005GL023941).
- HOEK, E. and DIEDERICHS, M. S. (2006), *Empirical estimation of rock mass modulus*, *Int. J. Rock Mech. Min. Sci.* 43, 203–215.
- HUDSON, J. A. (1980), *Overall properties of a cracked solid*. Cambridge Phil. Soc., Math. Proc. 88, 371–384.
- HUDSON, J. A., LIU, R., and CRAMPIN, S. (1996), *The mechanical properties of materials with interconnected cracks and pores*, *Geophys. J. Int.* 124, 105–112.
- JAEGER, J. C., COOK, N. G. W., and ZIMMERMANN, R. W. (2007), *Fundamentals of Rock Mechanics* (Blackwell Publishing, Malden, MA, U.S.A., 2007).
- KACHANOV, M. (1992), *Effective elastic properties of cracked solids: Critical review of some basic concepts*, *Appl. Mech. Rev.* 45, 304–335.
- LACHENBRUCH, A. H. (1980), *Frictional heating, fluid pressure, and the resistance to fault motion*, *J. Geophys. Res.* 85, 6097–6112.
- LAURSEN, T. A. *Computational contact and impact mechanics* (Springer-Verlag, Berlin and Heidelberg 2002).
- LAURSEN, T. A. and SIMO, J. C. (1993), *A continuum-based finite element formulation for the implicit solution of multibody large deformation frictional contact problems*, *Int. J. Num. Meth. Eng.* 36, 3451–3485.
- LI, Y.-G., AKI, K., ADAMS, D., HASEMI, A., and LEE, W. H. K. (1994), *Seismic guided waves trapped in the fault zone of the Landers, California, earthquake of 1992*, *J. Geophys. Res.* 99, 11,705–11,722.
- LOCKNER, D., TANAKA, H., ITO, H., and IKEDA, R. (2000), *Permeability and strength of core samples from the Nojima fault of the 1995 Kobe earthquake*. In *Proc. Internat. Workshop on the Nojima Fault Core and Borehole Analysis*, U.S. Geological Survey Open-file Report 00-129.

- LOCKWOOD, J. P. and LYDON, P. A. (1975), *Geologic map of the Mount Abbot quadrangle, California*. Geological Survey Geologic Quadrangle GQ-1155 scale 1:62,500.
- LYAKHOVSKY, V. and BEN-ZION, Y. (2008), *Scaling relations of earthquakes, aseismic deformation and evolving fault structures in a damage rheology model*, *Geophys. J. Int.*, **172**, 651–662, doi: [10.1111/j.1365-246X.2007.03652.x](https://doi.org/10.1111/j.1365-246X.2007.03652.x).
- LYAKHOVSKY, V., BEN-ZION, Y., and AGNON, A. (1997a), *Distributed damage, faulting, and friction*, *J. Geophys. Res.* **102**, 27635–27649.
- LYAKHOVSKY, V., RECHES, Z., WEINBERGER, R., and SCOTT, T. E. (1997b), *Non-linear elastic behaviour of damaged rocks*, *Geophys. J. Int.*, 157–166.
- MAHTAB, M. A. (1969), *Three-dimensional finite element analysis of joint and rock slopes*. Ph.D. Thesis, Univ. of California, Berkeley.
- MARTEL, S. J., POLLARD, D. D., and SEGALL, P. (1988), *Development of simple strike-slip fault zones, Mount Abbot Quadrangle, Sierra Nevada, California*. *Geol. Soc. Am. Bull.* **100**, 1,451–1,465.
- MARTEL, S. J. and POLLARD, D. D. (1989), *Mechanics of slip and fracture along small faults and simple strike-slip fault zones in granitic rock*, *J. Geophys. Res.* **94**, 9,417–9,428.
- MARTEL, S. J. (1990), *Formation of compound strike-slip fault zones, Mount Abbot quadrangle, California*, *J. Struct. Geol.* **12**, 869–882.
- MARTEL, S. J. and BOGER, W. A. (1998), *Geometry and mechanics of secondary fracturing around small three-dimensional faults in granitic rock*. *J. Geophys. Res.* **103**, 21,299–21,314.
- MASE, C. W. and SMITH, L. (1987), *Effects of frictional heating on the thermal, hydrologic, and mechanical response of a fault*, *J. Geophys. Res.* **92**, 6249–6272.
- MAVKO, G., MUKERJI, T., and DVORKIN, J. *The Rock Physics Handbook; Tools for Seismic Analysis in Porous Media* (Cambridge University Press 1998).
- MYERS, R. and AYDIN, A. A. (2004), *The evolution of fault zones formed by shearing across joint zones in sandstone*, *J. Struct. Geol.* **26**, 947–956.
- NODA, H. and SHIMAMOTO, T. (2005), *Thermal pressurization and slip-weakening distance of a fault: An example of the Hanaore Fault, southwest Japan*, *Bull. Seismol. Soc. Am.* **95**(4), 1224–1233.
- O'CONNELL, R. J. and BUDIANSKI, B. (1974), *Seismic velocities in dry and wet cracked solids*, *J. Geophys. Res.* **79**, 5412–5426.
- PACHELL, M. A. and EVANS, J. P. (2002), *Growth, linkage, and termination processes of a 10-km-long, strike-slip fault in jointed granite: The Gemini fault zone, Sierra Nevada, California*. *J. Struct. Geol.* **24**, 1903–1924.
- POLLARD, D. D. and SEGALL, P. *Theoretical displacements and stresses near fractures in rock: With applications to faults, joints, veins, dikes, and solution surfaces*. In *Fracture Mechanics of Rock* (ed. B. K. Atkinson), pp. 277–349 (Academic Press Inc. 1987).
- RENSHAW, C. E. (1997), *Mechanical controls on the spatial density of opening-mode fracture networks*, *Geology* **25**(10), 923–926.
- RICE, J. R. (2006), *Heating and weakening of faults during earthquake slip*, *J. Geophys. Res.* **111**, doi:[10.1029/2005JB004006](https://doi.org/10.1029/2005JB004006).
- ROSSO, R. (1976), *A comparison of joint stiffness measurements in direct shear, triaxial compression and in situ*, *Int. J. Rock Mech. Min. Sci. Geomech. Abst.* **13**, 167–172.
- SANZ, P. F. (2008), *Modeling rock folding with large deformation frictional contact mechanics*, Ph.D. Thesis, Stanford University, California, USA.
- SANZ, P. F., BORJA, R. I., and POLLARD, D. D. (2007), *Mechanical aspects of thrust faulting driven by far-field compression and their implications to fold geometry*, *Acta Geotech.* **2**, 17–31.
- SANZ, P. F., POLLARD, D. D., ALLWARDT, P. F., and BORJA, R. I. (2008), *Mechanical models of fracture reactivation and slip on bedding surfaces during folding of the asymmetric anticline at Sheep Mountain, Wyoming*, *J. Struct. Geol.* **30**, 1177–1191, doi:[10.1016/j.jsg.2008.06.002](https://doi.org/10.1016/j.jsg.2008.06.002).
- SCHULTZ, S. E. and EVANS, J. P. (2000), *Mesosopic structure of the Punchbowl Fault, Southern California and the geologic and geophysical structure of active strike-slip faults*, *J. Struct. Geol.* **22**, 913–930.
- SEGALL, P. and POLLARD, D. D. (1983a), *Nucleation and growth of strike slip faults in granite*, *J. Geophys. Res.* **88**, 555–568.
- SEGALL, P. and POLLARD, D. D. (1983b), *Joint formation in granitic rock of the Sierra Nevada*, *Geol. Soc. Am. Bull.* **94**, 563–575.

- SEGALL, P., MCKEE, E. H., MARTEL, S. J., and TURRIN, B. D. (1990), *Late Cretaceous age of fractures in the Sierra Nevada batholith, California*, *Geology* 18, 1,248–1,251.
- SIBSON, R. H. (1973), *Interactions between temperature and pore-fluid pressure during earthquake faulting and a mechanism for partial or total stress relief*, *Nature* 243, 66–68.
- SIMO, J. C. and TAYLOR, R. L. (1985), *Consistent tangent operators for rate-independent elastoplasticity*, *Computer Methods in Applied Mechanics and Engineering* 48, 101–118.
- SONMEZ, H., GOKCEOGLU, C., NEFESLIOGLU, H. A., KAYABASI, A. (2006), *Estimation of rock modulus: For intact rocks with an artificial neural network and for rock masses with a new empirical equation*, *Int. J. Rock Mech. Min. Sci.* 43, 224–35.
- STERN, T. W., BATEMAN, P. C., MORGAN, B. A., NEWALL, M. F., and PECK, D. L. (1981), *Isotopic U-Pb ages of zircon from the granitoids of the central Sierra Nevada, California*, *U.S. Geol. Surv. Prof. Paper* 1185, 17.
- WALSH, J. B. (1965), *The effect of cracks on the uniaxial elastic compression of rocks*, *J. Geophys. Res.* 70, 399–411.
- WEINBERGER, R., RECHES, Z., EIDELMAN, A., and SCOTT, T. S. (1994), *Tensile properties of rocks in four-point beam tests under confining pressure*. In *Proc. the First North American Rock Mechanics Symp.*, Austin, Texas, (eds. P. Nelson and S.E. Laubach), pp. 435–442.
- WIBBERLEY, C. A. J. (2002), *Hydraulic diffusivity of fault gouge zones and implications for thermal pressurization during seismic slip*, *Earth Planets Space* 54, 1153–1171.
- WIBBERLEY, C. A. J. and SHIMAMOTO, T. (2003), *Internal structure and weakening effects of major strike-slip fault zones: The Median Tectonic Line in Mie Prefecture, Southwest Japan*, *J. Struct. Geol.* 25, 59–78.
- WORTHINGTON, M. H. and LUBBE, R. (2007), *The scaling of fracture compliance*, *Geol. Soc. Lond. Spec. Pub.* 207, 73–82.
- WRIGGERS, P. (1995), *Finite-element algorithms for contact problems*, *Arch. Comput. Meth. Eng.* 4, 1–49.
- WRIGGERS, P., *Computational Contact Mechanics* (Wiley and Sons 2002).
- WU, H. and POLLARD, D. D. (1995), *An experimental study of the relationship between joint spacing and layer thickness*, *J. Struct. Geol.* 17(6), 887–905.
- YOSHIOKA, N. and SCHOLZ, C. H. (1989), *Elastic properties of contacting surfaces under normal and shear loads 1. Theory*, *J. Geophys. Res.* 94, 17681–17690.
- YOSHIOKA, N. and SCHOLZ, C. H. (1989), *Elastic properties of contacting surfaces under normal and shear loads 2. Comparison of Theory with Experiment*, *J. Geophys. Res.* 94, 17691–17700.
- ZOBACK, M. D. and BYERLEE, J. D. (1975), *The effect of microcrack dilatancy on the permeability of Westerly granite*, *J. Geophys. Res.* 80, 752–755.

(Received August 14, 2008, revised January 26, 2009)

Published Online First: June 27, 2009

To access this journal online:
www.birkhauser.ch/pageoph
